UNIVERSITY OF CALIFORNIA, SAN DIEGO

Prediction of Inertial Confinement Fusion Chamber Gas Evolution using Multi-species Computational Fluid Dynamics

A thesis submitted in partial satisfaction of the
requirements for the degree Master of Science

in

Engineering Sciences (Aerospace Engineering)

by

Robert Scott Martin

Committee in charge:

Farrokh Najmabadi, Chair
Zoran Dragojlovic
Forman A. Williams

2007

.

The thesis of Robert Scott Martin is approved:

Chair

University of California, San Diego

2007

TABLE OF CONTENTS

LIST OF FIGURES

LIST OF TABLES

ABSTRACT OF THE THESIS

Prediction of Inertial Confinement Fusion Chamber Gas Evolution
using Multi-species Computational Fluid Dynamics

by

Robert Scott Martin

Masters of Science in Engineering Sciences (Aerospace Engineering)

University of California, San Diego, 2007

Farrokh Najmabadi, Chair

Inertial confinement fusion is one of two primary approaches to the production of fusion energy for power generation. Due to the high cost of experimentation for large scale systems such as Laser Inertial Fusion Energy (Laser IFE), the ability to accurately simulate the expected performance using properly validated models is of critical importance.

The evolution of the chamber environment from target injection through the generation of fusion energy is a critical issue for the success of Laser IFE. In the research presented, the output of a radiation hydrodynamics code is used as the initial condition for evolving the chamber gas dynamics up until a subsequent target injection. To perform these simulations, our group has developed a 2D/3D-Axisymmetric Navier-Stokes fluids code that includes an additional radiation source term. The work presented here has been to extend this code to include the effects of multiple gas species and higher order mechanisms such as diffusion from the Dufour and Soret effects.

Validation of the numerical method is demonstrated in the case of separation of Helium and Xenon gas in a shock wave. It is also shown that the code uses reasonably accurate transport coefficients for He:Xe mixtures based on curve fits produced by the ChemKin preprocessor. Numerical simulations of the Laser IFE configuration using the augmented system track the mixing of the Xe gas in the chamber with cold Xe gas from jets on the wall. Simulations using cold He:Xe mixture jets of varying composition are also investigated.

Chapter I

Introduction

I.A Background

Inertial and magnetic confinement fusion are the two primary approaches to the production of fusion energy for power generation. For laser inertial fusion energy (Laser IFE), an array of intense lasers symmetrically and directly illuminates a cryogenic target of hydrogen isotopes that has been injected into a vacuum chamber. The target is compressed and heated to undergo thermonuclear burn. The energy released by the target is recovered by the chamber wall and converted into electricity. This process is repeated 5-10 times per second. Due to the high cost of experimentation for large scale systems such as Laser IFE, the ability to accurately simulate the expected performance using properly validated models has never before been so vital.

Though current IFE designs include minimal chamber pressure, a small amount of gas remains within the chamber to act as a buffer for the intense energy burst resulting from the fusion burn. Because of its superior ability to absorb x-rays and re-emit radiation, Xenon gas was selected as this buffer gas. The evolution of the chamber environment from target injection to the generation of fusion energy is a critical issue for the success of IFE. In the research presented, the output from "BUCKY", a radiation hydrodynamics code which simulates the target

implosion and fusion energy release, is used as the initial condition for evolving the chamber gas dynamics from 0.0005s-0.1s. To perform these simulations, our group has developed a 2D/3D-Axiisymetric Navier-Stokes code with an additional radiation source term. The code uses a second order Godunov method on a uniform adaptively refined mesh with an embedded boundary. The current work has been to extend this code to include the effects of multiple gas species and higher order mechanisms such as diffusion from the Dufour and Soret effects.

I.B Physical Setting

I.B.1 Continuum Approximation

Before developing the fluid equations in the subsequent sections, it is important to investigate the validity of the continuum approximation in the proposed application of Laser IFE. To achieve this goal, the Knudsen number seen in Equation I.1 must first be defined. In this equation, λ_{mfp} is the mean free path as defined in Equation I.2 from Reference [24] and L is a characteristic length scale of the boundaries. A flow is called "free-molecular flow" if $\mathcal{K} \geqq 1$. If this is the case, statistical mechanics rather than continuum mechanics should be used to describe the fluid dynamics of the system.

In the initial output from "BUCKY" using pure Xenon background gas at a density corresponding to 50 milli-torr pressure at 0^oC, the maximum mean free path is $2.15cm$ near the center of a $10m$ chamber. The Knudsen number of 0.00215 indicates that, despite the low chamber density, continuum mechanics may still be used on the chamber.

The details of the flowfield around smaller scale features such as the $1m$ wide beam lines would be more in question, but the flowfield is originally uniform and symmetric near the walls with a mean free path 14 times smaller. The $2.15cm$ mean free path is the result of very low density region in the chamber center created by the fusion burn. The features of the flowfield therefore remain large where the

mean free path is large.

However, for a $4mm$ diameter IFE target, the $2.15cm$ mean free path corresponds to a Knudsen number of 5.38. Even after $100ms$, the Knudsen number for the target remains a relatively high 0.9 in some parts of the chamber. This implies that, though the continuum treatment for the full chamber and even beam lines is reasonable, it should not be applied to the target.

$$\mathcal{K} = \frac{\lambda_{mfp}}{L} \tag{I.1}$$

$$\lambda_{mfp} = \frac{\mu}{\rho}\sqrt{\frac{\pi m}{2kT}} \tag{I.2}$$

I.B.2 Conservation Equations

Because basic particle collisions conserve mass, momentum and energy, these quantities are preserved for the sum of all possible collisions within a fluid. The fluid equations are the result of integrating these conserved quantities as the moments m, mv_i, and $\frac{1}{2}mv^2$ against the Boltzmann equation, Equation I.3, as shown in Equation I.4 where $Q(v_i)$ represents these moments. The resulting equations per unit volume for each of the conserved quantities respectively yields Equations I.5 - I.7 as outlined in Chapter IX of Vincenti, [24]. In all of these equations, the overbar notation refers to an average over the distribution function as shown in Equation I.8. Indices i, j, k refer summation notation over spacial dimensions and indices q, r, s refer to gas species numbered from $1 - S$.

$$\frac{\partial}{\partial t}(nf(v_i)) + v_j\frac{\partial}{\partial x_j}(nf(v_i)) + \frac{\partial}{\partial v_j}(F_j nf(v_i)) = \left\{\frac{\partial}{\partial t}(nf(v_i))\right\}_{coll} \tag{I.3}$$

$$\int_{-\infty}^{\infty} Q(v_i)\left[\frac{\partial(nf)}{\partial t} + v_j\frac{\partial(nf)}{\partial x_j} + \frac{\partial(F_j nf)}{\partial v_j}\right]dv_i = \int_{-\infty}^{\infty} Q(v_i)\left[\left\{\frac{\partial(nf)}{\partial t}\right\}_{coll}\right]dv_i \tag{I.4}$$

$$\frac{\partial \rho}{\partial t} + \frac{\partial}{\partial x_j}[\rho \overline{v}_j] = 0 \tag{I.5}$$

$$\frac{\partial}{\partial t}[\rho \overline{v}_i] + \frac{\partial}{\partial x_j}[\rho \overline{v_i v_j}] = \rho \overline{F_i} \tag{I.6}$$

$$\frac{1}{2}\frac{\partial}{\partial t}[\rho \overline{v^2}] + \frac{1}{2}\frac{\partial}{\partial x_j}[\rho \overline{v_j v^2}] = \rho \overline{F_j v_j} \tag{I.7}$$

$$\overline{Q} \equiv \int_{-\infty}^{\infty}\int_{-\infty}^{\infty}\int_{-\infty}^{\infty} Q(v_i) f dv_1 dv_2 dv_3 \tag{I.8}$$

With proper definitions for the pressure, stress tensor, heat flux vector, temperature, and total specific energy these equations reduce to the familiar Navier-Stokes equations for flows sufficiently close to local equilibrium. When these equations are extended to multiple species, collision integrals for the interactions between the species must be included. However, when the moments of mass, momentum, and energy are taken, the equations can again be simplified because the quantities are conserved in collisions. The resulting set of equations include species conservation, total momentum conservation, and total energy conservation as shown in Equations I.10-I.12 subject to definitions in Equation I.9.

$$\begin{aligned}
\rho v_{0i} &\equiv \sum_{s=1}^{S} \rho_s (\overline{v_i})_s \\
V_i &\equiv v_i - v_{0i} \\
\frac{3}{2}kT &= \frac{1}{n}\sum_{s=1}^{S}\frac{1}{2} n_s m_s (\overline{V^2})_s \\
p &\equiv \sum_{s=1}^{S} p_s = nkT \\
\tau_{ij} &\equiv \sum_{s=1}^{S} (\tau_{ij})_s \\
q_i &\equiv \sum_{s=1}^{S} (q_i)_s \\
e_t &\equiv e + \frac{1}{2}v_0^2 = c_v T + \frac{1}{2}v_0^2
\end{aligned} \tag{I.9}$$

$$\frac{\partial}{\partial t}[\rho_s] + \frac{\partial}{\partial x_j}[\rho_s v_{0j} + \rho_s(\overline{V}_j)_s] = 0 \tag{I.10}$$

$$\frac{\partial}{\partial t}[\rho v_{0i}] + \frac{\partial}{\partial x_j}[P\delta_{ij} + \rho v_{0i} v_{0j}] = \frac{\partial \tau_{ij}}{\partial x_j} + \sum_{s=1}^{S} \rho_s(\overline{F_i})_s \tag{I.11}$$

$$\frac{\partial}{\partial t}[\rho e_t] + \frac{\partial}{\partial x_j}[v_{0j}(P + \rho e_t)] = \frac{\partial}{\partial x_j}[\tau_{kj} v_{0k} - q_j] + \sum_{s=1}^{S} \rho_s(\overline{F_{sj} v_j})_s \tag{I.12}$$

Diffusion

The concept of diffusion velocity is the result of considering the mass average bulk velocity separate from the random noise. This random noise is in fact closely tied to the concept of temperature as shown in the preceeding definitions. For multi-species fluid dynamics, the species average diffusion velocity, $(\overline{V}_i)_s$, is defined in Equation I.13 by summing over N_s molecules of class s. For this reason, though the density weighted sum of species average diffusion velocities, $\sum_s^S \rho_s V_{is}$, is zero by definition, the individual species average diffusion velocities are not necessarily. In fact, resulting from imbalances in the random velocities for different classes of molecules, these diffusion velocities result in the classical concept of Fickian diffusion due to concentration gradients as well as higher order phenomena such as thermal diffusion resulting from different sound speeds in molecules of different mass.

$$V_{is} = (\overline{V}_i)_s = \frac{1}{N_s} \sum_{n=1}^{N_s} m_n V_{ni} \tag{I.13}$$

An equation for the diffusion velocity, V_{is}, can be written in terms of a generalized concentration gradient vector, d_{is}, and temperature gradient as shown in Equation I.14. The form of the generalized concentration gradient is shown in Equation I.15. The diffusion velocities depend on multi-species diffusion coefficients, D_{sr}, and coefficients of thermal diffusion, D_s^T. These coefficients can be derived using a Chapman-Enskog expansion of the Boltzmann equation in So-

nine polynomials as shown in Reference [13]. Equations I.16 and I.17 give the multi-species diffusion coefficient and coefficient of thermal diffusion respectively.

Because of the orthogonality of the Sonine polynomials, the resulting expressions for the diffusion coefficients depend only upon one Sonine expansion coefficient each, $c_{s0}^{(r,s)}(\xi)$ and $a_{s0}(\xi)$. However, the value of the expansion coefficients is dependant on the number of terms taken in the expansion, ξ. For multi-species diffusion, taking $\xi = 1$ is sufficient, but for thermal diffusion, ξ must be greater than or equal to 2 for the coefficient to be nonzero.

The Sonine polynomial expansion depends on the true distribution function being reasonably represented by perturbations from equilibrium in the Sonine polynomials. This requires that averages be taken over a sufficient number of collisions as to ensure the validity through the central limit theorem. This results in a strengthening of the continuum constraint on the Knudsen number. However, as long as the fluid properties only vary slightly over $10s$ of mean free paths, the results are likely to be reasonably valid.

The Sonine expansion coefficients may be evaluated by solving sets of linear equations that use tabulated collision integral data, $\Omega_{sr}^{(m,n)}$ for specified potential representations of the molecules such as the Jones (6-12) potential. This approach has some limitations such as the Jones potential being spherical and therefore unable to fully represent polyatomic gases. Hirschfelder, Curtiss, and Bird, Reference [13], also show a method of converting binary diffusion coefficients to multi-species diffusion coefficients as shown in Equations I.19 and I.21 where F^{sr} is the cofactor of F_{sr} in the determinant of $|F|$ as shown in Equation I.20. In Equation I.19, $\mathcal{D}_{sr}$ is the diffusion coefficient for a binary mixture. Using this approach, experimental data based on binary diffusion can be used when available and the system can be completed if necessary using the estimated coefficients.

Rather than reporting the thermal diffusion coefficient directly, most experimental data available uses the thermal diffusion ratio, k_T, as defined in Equation I.18 for binary mixture AB. This is because classical examples of thermal

diffusion are typically performed in binary, incompressible, steady state settings where k_T is more natural. However, because the IFE system has strong thermal gradients, an investigation into the relative contribution of the effect needs to be done. As explained later in the implementation section, the concept of the thermal diffusion ratio is used in the case of a light gas diffusing through a heavier gas mixture as a first approximation to thermal diffusion.

$$V_{is} = \left(\frac{n^2}{n_s \rho}\right) \sum_{r=1}^{S} m_r D_{sr} d_{ir} - \frac{1}{n_s m_s} D_s^T \frac{\partial \ln T}{\partial x_i} \tag{I.14}$$

$$d_{is} = \frac{\partial}{\partial x_i}\left(\frac{n_s}{n}\right) + \left(\frac{n_s}{n} - \frac{n_s m_s}{\rho}\right) \frac{\partial \ln p}{\partial x_i} - \left(\frac{n_s m_s}{P\rho}\right) \left[\frac{\rho}{m_s} F_{is} - \sum_{r=1}^{S} n_r F_{ir}\right] \tag{I.15}$$

$$D_{rs}(\xi) = \frac{\rho n_s}{2 n m_r} \sqrt{\frac{2kT}{m_s}} c_{s0}^{(r,s)}(\xi) \tag{I.16}$$

$$D_s^T(\xi) = \frac{n_s m_s}{2} \sqrt{\frac{2kT}{m_s}} a_{s0}(\xi) \tag{I.17}$$

$$k_T = \frac{\rho}{n^2 m_A m_B} \frac{D_A^T}{\mathcal{D}_{AB}} \tag{I.18}$$

$$F_{sr} = \left\{ \frac{n_s}{\rho \mathcal{D}_{sr}(1)} + \sum_{q=1, q\neq r}^{S} \frac{n_q m_q}{\rho m_i \mathcal{D}_{sq}(1)} \right\} (1 - \delta_{sr}) \tag{I.19}$$

$$F^{sr} = (-1)^{s+r} \begin{vmatrix} F_{11} & \cdots & F_{1,r-1} & F_{1,r+1} & \cdots & F_{1\nu} \\ \cdot & & \cdot & \cdot & & \cdot \\ \cdot & & \cdot & \cdot & & \cdot \\ \cdot & & \cdot & \cdot & & \cdot \\ F_{s-1,1} & \cdots & F_{s-1,r-1} & F_{s-1,r+1} & \cdots & F_{s-1,\nu} \\ F_{s+1,1} & \cdots & F_{s+1,r-1} & F_{s+1,r+1} & \cdots & F_{s+1,\nu} \\ \cdot & & \cdot & \cdot & & \cdot \\ \cdot & & \cdot & \cdot & & \cdot \\ \cdot & & \cdot & \cdot & & \cdot \\ F_{\nu,1} & \cdots & F_{\nu,r-1} & F_{\nu,r+1} & \cdots & F_{\nu,\nu} \end{vmatrix} \tag{I.20}$$

$$D_{sr}(1) = \frac{F^{sr} - F^{ss}}{m_r |F|} \tag{I.21}$$

Shear

The viscous forces on the gas come into the momentum and energy equations through the shear tensor, τ_{ij}. For a multi-species gas, the shear tensor has the form shown in Equation I.22. In the equation, μ is the coefficient of viscosity, S is the stress tensor, and κ is the coefficient of bulk viscosity.

The bulk viscosity is zero for all monatomic gases as it has to do with the rate of transfer of kinetic energy to the internal energy states. For polyatomic gasses, the equation for the bulk viscosity requires relaxation times for the energy transfer to the internal degrees of freedom.

Reference [13] provide a means of calculating the coefficient of viscosity similar to that of calculating the diffusion coefficients from the Enskog expansion. The resulting expression for the coefficient is shown in Equation I.23.In this equation, b_{s0} is another Sonine expansion coefficient. Like the multi-species diffusion coefficient, $\xi = 1$ is sufficient to calculate the viscosity coefficient to a reasonable

accuracy.

$$\tau_{ij} = -2\mu S_{ij} + (\frac{2}{3}\mu - \kappa\frac{\partial v_{0k}}{\partial x_k}\delta_{ij} \tag{I.22}$$

$$\mu(\xi) = \frac{1}{2}kT\sum_{s=1}^{S} n_s b_{s0}(\xi) \tag{I.23}$$

Heat Flux

The heat flux vector can also be evaluated using the techniques of Reference [13]. The resulting equation is shown in Equation I.24. In the equation, the diffusion velocities, V_{is}, coefficient of thermal diffusion, D_s^T, and generalized concentration gradient, d_{is}, defined earlier are again used. In addition, the coefficient of thermal conductivity, λ_0 is used as defined in Equation I.25. In this equation, a_{s1} is yet another of the Sonine expansion coefficients.

Equations I.24 and I.25 show heat fluxes in terms of λ_0, but λ_0 is not the normal definition of thermal conductivity. Equation I.26 from Reference [13], shows the heat flux in terms of the normal λ. Equation I.27, show the relationship between λ and λ_0. Though this looks like a complication, using the heat flux vector in this form allows for direct comparison between analytical and experimentally reported values for λ.

This form of the heat flux vector does not include radiation contributions already present in the code. The heat flux vector was also derived for a monatomic gas. Hirschfelder, Curtis, and Bird do derive the equations for polyatomic gas mixtures, but these corrections have not yet been included in the formulation.

$$q_i = \frac{5}{2}kT\sum_s n_s V_{is} - \lambda_0\frac{\partial T}{\partial x_i} - nkT\sum_{s=1}^{S}\frac{1}{n_s m_s}D_s^T d_{is} \tag{I.24}$$

$$\lambda_0(\xi) = -\frac{5}{4}k\sum_s n_s\sqrt{\frac{2kT}{m_s}}a_{s1}(\xi) \tag{I.25}$$

$$q_i = \frac{5}{2}kT\sum_s n_s V_{is} - \lambda\frac{\partial T}{\partial x_i} - \frac{kT}{n}\sum_{r,s=1}^{S}\frac{n_s D_r^T}{m_r \mathcal{D}_{rs}}\left(V_{ir} - V_{is}\right) \tag{I.26}$$

$$\lambda = \lambda_0 - \frac{k}{2n}\sum_{r,s=1}^{S}\frac{n_r n_s}{\mathcal{D}_{rs}}\left[\frac{D_r^T}{n_r m_r} - \frac{D_s^T}{n_s m_s}\right] \tag{I.27}$$

Chapter II

Implementation

II.A Numerical Methods

A derivation of the numerical method used in the IFE simulations follows. The algorithm presented is an extension of the work of Dragojlovic and Najmabadi in Reference [7]. This finite-volume algorithm for the Navier-Stokes equations uses a discrete conservative update based on a time-explicit Godunov method for inviscid fluxes and a two-step Runge-Kutta update for viscous fluxes. It also incorporates a nonuniform boundary embedded in a uniform cartesian mesh. For further details of this algorithm such as the embedded boundary, the reader should consult Reference [17].

Conservation Form

In order to accurately simulate fluid flow, it is helpful to rewrite the Navier-Stokes Equations I.5-I.7 in terms of conservative variables and fluxes as shown in Equation II.1. In the equation, U is the state vector, $\bar{\bar{F}}_I$ is the inviscid flux dyadic, $\bar{\bar{F}}_V$ is the viscous flux dyadic, and S is the source term from effects such as body forces.

$$\frac{\partial U}{\partial t} + \frac{\partial}{\partial x_i}\left[\bar{\bar{F}}_I - \bar{\bar{F}}_V\right] = S \tag{II.1}$$

$$U = \begin{Bmatrix} \rho \\ \rho\vec{v} \\ \rho e_t \end{Bmatrix} \quad \bar{\bar{F}}_I = \begin{Bmatrix} \rho\vec{v} \\ p\bar{\bar{I}} + \rho\vec{v}\vec{v} \\ (p+\rho e_t)\vec{v} \end{Bmatrix} \quad \bar{\bar{F}}_V = \begin{Bmatrix} \vec{0} \\ \bar{\bar{\tau}} \\ \vec{v}\cdot\bar{\bar{\tau}} + k\nabla T \end{Bmatrix}$$

The multi-species equations developed here extend this conservation form of the equations by adding $s-1$ species conservation equations to the set where s is the number of species in the fluid. The last species governing equation is redundant with the others and the overall continuity equation and is therefore neglected from the system. This combination is preferred over using s species governing equations without the continuity equation because the continuity equation is an expression of the conservation of mass whereas if chemical reactions are included the individual species governing equations are not necessarily conservative. Solving the continuity equation also requires fewer operations.

$$U = \begin{Bmatrix} \rho \\ \rho\vec{v}_0 \\ \rho e_t \\ \rho_1 \\ \cdot \\ \cdot \\ \cdot \\ \rho_{s-1} \end{Bmatrix} \quad \bar{\bar{F}}_i = \begin{Bmatrix} \rho\vec{v}_0 \\ p\bar{\bar{I}} + \rho\vec{v}_0\vec{v}_0 \\ (p+\rho e_t)\vec{v}_0 \\ \rho_1\left(\vec{v}_0 + \vec{V}_1\right) \\ \cdot \\ \cdot \\ \cdot \\ \rho_{s-1}\left(\vec{v}_0 + \vec{V}_{s-1}\right) \end{Bmatrix} \quad \bar{\bar{F}}_v = \begin{Bmatrix} \vec{0} \\ \bar{\bar{\tau}} \\ \vec{v}_0\cdot\bar{\bar{\tau}} + k\nabla T - \frac{5}{2}kT\sum_s n_s\vec{V}_s \\ \vec{0} \\ \cdot \\ \cdot \\ \cdot \\ \vec{0} \end{Bmatrix} \tag{II.2}$$

However in practice, the full set of s species conservation equations were calculated and projected back onto the mass conservative manifold using equation II.3 to ensure consistent treatment of all the species. The differential equations are also actually solved in their weak form as shown in Equation II.4. Because the

equations are in conservative form, only information about the fluxes on the cell boundaries in time and space as well as any volumetric source terms in time are needed to calculate the cell averaged state variables for all time.

$$\rho_s = \rho_s \frac{\rho}{\sum_{r=1}^{S} \rho_r} \tag{II.3}$$

$$\int_\Omega \frac{\partial U}{\partial t} d\Omega + \int_{\partial\Omega} [\bar{\bar{F}}_I - \bar{\bar{F}}_V] \cdot \vec{n}\, dA = \int_\Omega S d\Omega \tag{II.4}$$

In the codes, the inviscid portion of the fluxes are solved first using an explicit linearization shown in Equation II.5. The multidimensional flux is considered as a sum of fluxes resulting from solving 1D Riemann problems in the coordinate directions forward in time. In the weak from, this can be seen as an assumption that the contribution to the fluxes result only from the jump normal to the computational cell face. According to Reference [22], this is a reasonable approximation as long as the grid is nearly orthogonal. In Equation II.5, L and R are the left and right eigenvectors and Λ is the diagonal matrix of eigenvalues such that $L\Lambda R$ is equal to the flux Jacobian $\frac{\partial \bar{\bar{F}}_I}{\partial U}$. Because $R = L^{-1}$ and R and L are constant with respect to t and x within the linearization, pre-multiplication of Equation II.5 by R yields Equation II.6 where $W = RU$. Because Λ is diagonal, this then yields a set of q decoupled scalar equations as shown in II.7 where summation notation is not implied. Figure II.1 shows a graphical representation of this hyperbolic portion of the problem for a sample representative configuration solved forward in time in one dimension.

$$\frac{\partial U}{\partial t} + \frac{\partial \bar{\bar{F}}_I}{\partial x} = \frac{\partial U}{\partial t} + \frac{\partial \bar{\bar{F}}_I}{\partial U}\frac{\partial U}{\partial x} = \frac{\partial U}{\partial t} + [L\Lambda R]\frac{\partial U}{\partial x} = 0 \tag{II.5}$$

$$R\frac{\partial U}{\partial t} + R[L\Lambda R]\frac{\partial U}{\partial x} = \frac{\partial [RU]}{\partial t} + I\Lambda\frac{\partial [RU]}{\partial x} = \frac{\partial W}{\partial t} + \Lambda\frac{\partial W}{\partial x} = 0 \tag{II.6}$$

$$\frac{\partial w_q}{\partial t} + \lambda_q \frac{\partial w_q}{\partial x} = 0 \tag{II.7}$$

For the multi-species versions of the Riemann solvers presented, the equation for the maximum time step, Equation II.8, remains the same as in the original single species versions. This constraint is commonly referred to as the CFL condition. In the equation, λ refers to the eigenvalues of the fluid equations. The maximum eigenvalue corresponds to the maximum rate at which information can propagate across a numerical cell. By limiting the time step as shown, disturbances cannot propagate across more than one numerical cell per time step. Because of the additional species governing equations, $s-1$ more eigenvalues are included when compared to the single species versions. Though these eigenvalues can be seen in Equation II.14 in the section on Roe's scheme, they are the same for both Riemann solvers. As mentioned earlier, in practice eigenvalues for all s species diffusion velocities are included in the time step limitation to ensure symmetry. Though the diffusion velocities depend on the states of the neighboring cells, because of the explicit linearization, it is not unreasonable for time steps limited by the CFL condition.

$$dt \leq \frac{dx}{|\lambda|_{max}} \tag{II.8}$$

The reason that a constant diffusion velocity across a timestep can be used is that the diffusion velocity is approximately proportional to the mean thermal velocity, mean free path, and a small constant due to the collision integral. For the spacial gradients to be physically meaningful, they must be taken as averages over several mean free paths. This makes the diffusion velocity approximately proportional to a small constant times the sound speed. Though this view is complicated in mixtures of species with significantly different masses, it is not unreasonable to imagine that, at the limit of maximum diffusion, the particles should not diffuse faster than their average thermal velocity using this model.

This line of thought leads directly to the concept of flux limiters. As mentioned in Reference [16], because the multi-species equations are derived for near equilibrium conditions, they can produce erroneously large fluxes for plasma

and strong shock-waves. This is because the continuum approximation is no longer valid for these conditions. However as mentioned in Reference [24], though the flow structures of sizes on the order of mean free paths may be incorrect for Navier-Stokes, this does not mean that the macro scale flow properties are incorrect because the equations are conservative. More on this topic can be found in the shock broadening validation section.

For these reasons a flux limiter for the multi-species mass and energy fluxes in the code was also investigated. The flux limiter was of the form suggested in Reference [16] and shown in Equations II.9 and II.10 where v_{th} corresponds to the thermal velocity. The thermal velocity is proportional to the sound speed up to a small constant as shown in Reference [24]. To ensure a smooth transition between normal and flux limited regions, an ad-hoc tan^{-1} transformation was applied as shown in Equation II.11. Figure II.2 shows a comparison between the original flux, F_0, and the limited flux, F_s for the tan^{-1} flux limiter. Though the limited flux necessarily deviates from the original flux, the important features are that the original and limited flux are tangent near zero flux and the limited flux asymptotically approaches the maximum flux at $\pm\infty$.

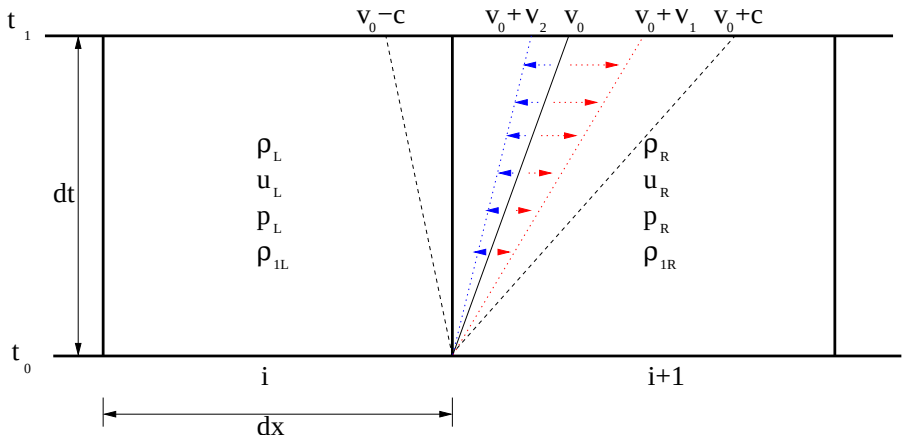

Figure II.1: Multi-species Riemann problem

$$F_{s,max} = \rho_s v_{th,s} \tag{II.9}$$

$$F_{\rho e,max} = \frac{P}{(\gamma - 1)} v_{th} \tag{II.10}$$

$$F = \frac{F_{max}}{\pi/2} tan^{-1}\left(\pi/2 \frac{F_0}{F_{max}}\right) \tag{II.11}$$

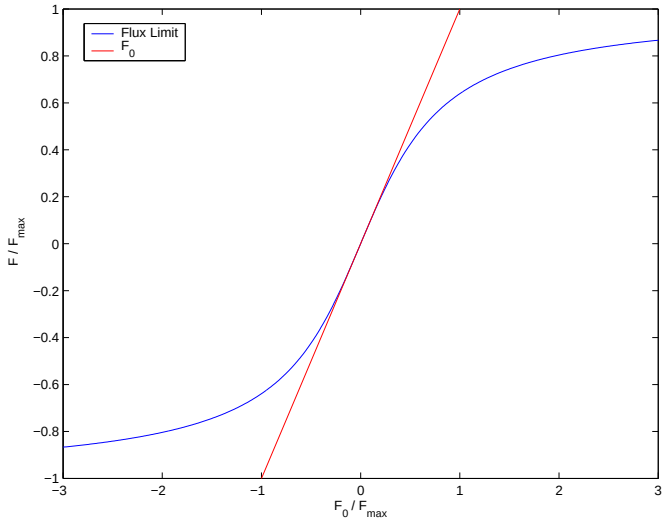

Figure II.2: Comparison between original and limited fluxes

Roe's Scheme

Roe's scheme is a popular approximate Riemann solver for Godunov's method [15]. Though the primary code used for the Inertial Fusion Energy chamber studies uses a more complicated Riemann solver for inviscid flux calculation, the mathematical analysis of fluid characteristics for the multi-species equations necessary to derive Roe's scheme helps justify the selection of multi-species fluxes used in the primary code.

Both Riemann solvers are based on similar assumptions and produced nearly identical results with a sufficiently fine grid for the 1D validation cases. However, the Roe's scheme implemented in the 1D code was missing the sonic entropy fix mentioned in Reference [15] and would therefore likely cause erroneous results in the case of a sonic rarefaction wave.

In implementing Roe's scheme, first the left and right states at the cell face were calculated. In order to achieve higher order accuracy, neighboring values were used to linearly project the states through the cell center to the face. However because this projection can lead to instability particularly with strong discontinuities, a minmod slope limiter was used. Reference [15] contains a section describing this and other slope-limiters in detail. This projection limits the face state variables such that they never exceed the range of the neighboring cell state variables.

The conservation equations are rewritten through the Jacobian of the flux as seen in equation II.12. For the multi-species code in 1D, the Jacobian, $\frac{\partial F}{\partial U}$, is an $[\,3+(s-1)\times 3+(s-1)]$ matrix. Because the diffusion velocities are complicated functions of the state variables, they are assumed to be approximately constant across the time step resulting in a purely explicit update.

The resulting Jacobian and eigenvalues with this and the perfect gas assumption are shown in Equation II.13. Once the eigenvalues, shown in Equation II.14, are known, the left and right eigenvector matrices can easily be derived and are shown in Equation II.15. In Roe's scheme, the Riemann problem for the flux

at the cell face, $i+\frac{1}{2}$, is decomposed into positive and negative direction waves using these eigenvalues and eigenvectors as shown in Equation II.16.

$$\frac{\partial U}{\partial t}+\frac{\partial F}{\partial U}\frac{\partial U}{\partial x}=0 \tag{II.12}$$

$$\frac{\partial F}{\partial U}=\begin{bmatrix} 0 & 1 & 0 & 0 & 0 & 0 \\ \frac{(\gamma-3)}{2}v_0^2 & -(\gamma-3)v_0 & (\gamma-1) & 0 & 0 & 0 \\ (\gamma-1)v_0^3-\gamma e_t v_0 & \gamma e_t-\frac{3}{2}(\gamma-1)v_0^2 & \gamma v_0 & 0 & 0 & 0 \\ -\frac{\rho_1 v_0}{\rho} & \frac{\rho_1}{\rho} & 0 & v_0+V_1 & 0 & 0 \\ -\frac{\rho_{...} v_0}{\rho} & \frac{\rho_{...}}{\rho} & 0 & 0 & v_0+V_{...} & 0 \\ -\frac{\rho_{s-1} v_0}{\rho} & \frac{\rho_{s-1}}{\rho} & 0 & 0 & 0 & v_0+V_{s-1} \end{bmatrix} \tag{II.13}$$

$$\lambda=\begin{bmatrix} v_0, & v_0+c, & v_0-c, & v_0+V_1, & v_0+V_{...}, & v_0+V_{s-1} \end{bmatrix} \tag{II.14}$$

$$R=\begin{bmatrix} \frac{1}{c} & \frac{1}{c} & \frac{1}{c} & 0 & 0 & 0 \\ \frac{v_0}{c} & \frac{v_0}{c}+1 & \frac{v_0}{c}-1 & 0 & 0 & 0 \\ \frac{v_0^2}{2c} & v_0+\frac{c}{\gamma-1}+\frac{v_0^2}{2c} & -v_0+\frac{c}{\gamma-1}+\frac{v_0^2}{2c} & 0 & 0 & 0 \\ 0 & \frac{\rho_1}{\rho(c-V_1)} & \frac{\rho_1}{\rho(c+V_1)} & 1 & 0 & 0 \\ 0 & \frac{\rho_{...}}{\rho(c-V_{...})} & \frac{\rho_{...}}{\rho(c+V_{...})} & 0 & 1 & 0 \\ 0 & \frac{\rho_{s-1}}{\rho(c-V_{s-1})} & \frac{\rho_{s-1}}{\rho(c+V_{s-1})} & 0 & 0 & 1 \end{bmatrix} \tag{II.15}$$

$$L=\begin{bmatrix} -\frac{(\gamma-1)v_0^2}{2c}+c & \frac{(\gamma-1)v_0}{c} & -\frac{\gamma-1}{c} & 0 & 0 & 0 \\ \frac{1}{2}\left(\frac{(\gamma-1)v_0^2}{2c}-v_0\right) & \frac{1}{2}\left(1-\frac{(\gamma-1)v_0}{c}\right) & \frac{\gamma-1}{2c} & 0 & 0 & 0 \\ \frac{1}{2}\left(\frac{(\gamma-1)v_0^2}{2c}+v_0\right) & \frac{1}{2}\left(-1-\frac{(\gamma-1)v_0}{c}\right) & \frac{\gamma-1}{2c} & 0 & 0 & 0 \\ -\frac{\rho_1}{\rho}\frac{\frac{(\gamma-1)}{2}v_0^2-v_0V_1}{c^2-V_1^2} & -\frac{\rho_1}{\rho}\frac{V_1-(\gamma-1)v_0}{c^2-V_1^2} & -\frac{\rho_1}{\rho}\frac{(\gamma-1)}{c^2-V_1^2} & 1 & 0 & 0 \\ -\frac{\rho_{...}}{\rho}\frac{\frac{(\gamma-1)}{2}v_0^2-v_0V_{...}}{c^2-V_{...}^2} & -\frac{\rho_{...}}{\rho}\frac{V_{...}-(\gamma-1)v_0}{c^2-V_{...}^2} & -\frac{\rho_{...}}{\rho}\frac{(\gamma-1)}{c^2-V_{...}^2} & 0 & 1 & 0 \\ -\frac{\rho_{s-1}}{\rho}\frac{\frac{(\gamma-1)}{2}v_0^2-v_0V_{s-1}}{c^2-V_{s-1}^2} & -\frac{\rho_{s-1}}{\rho}\frac{V_{s-1}-(\gamma-1)v_0}{c^2-V_{s-1}^2} & -\frac{\rho_{s-1}}{\rho}\frac{(\gamma-1)}{c^2-V_{s-1}^2} & 0 & 0 & 1 \end{bmatrix} \tag{II.15}$$

$$F_{i+\frac{1}{2}}=\frac{1}{2}\left\{F_i+F_{i+1}-[\hat{L}][|I\hat{\lambda}|][\hat{R}](U_{i+1}-U_i)\right\} \tag{II.16}$$

In Equation II.16, the hat symbol denotes that the eigenvalues and eigenvectors are calculated using a special "Roe-averaged state" weighted by Equation II.17. These relations in Equation II.18 are obtained by ensuring that Equation II.22 is satisfied. In the equation, h_t refers to the total specific enthalpy as defined in Equation II.21.

The absolute value in Equation II.16 is effectively up-winding for variables that result from decomposing the state based on the fluid characteristic lines. Further information on Roe's scheme is available in Reference [22].

It is important to note that satisfaction of Equation II.22 for the species conservation equations results in an equation for face species density that is singular when the left and right species densities are equal. This is a result of neglecting the diffusion velocity dependence on energy in the linearization of diffusion velocity. This deviation results in only partial upwinding in the species conservation equations. With these approximations, the face species density may be defined as in Equation II.20 in the analogous manner as the mixture face density. The diffusion velocities can then calculated for the face using the cell center values for needed gradients.

$$R_{i+\frac{1}{2}} = \sqrt{\frac{\rho_{i+1}}{\rho_i}} \tag{II.17}$$

$$\begin{aligned} \hat{\rho}_{i+\frac{1}{2}} &= R_{i+\frac{1}{2}}\rho_i \\ \hat{v}_{i+\frac{1}{2}} &= \frac{R_{i+\frac{1}{2}}v_{i+1} + v_i}{1 + R_{i+\frac{1}{2}}} \\ (\hat{h}_t)_{i+\frac{1}{2}} &= \frac{R_{i+\frac{1}{2}}(h_t)_{i+1} + (h_t)_i}{1 + R_{i+\frac{1}{2}}} \end{aligned} \tag{II.18}$$

$$S_{s,i+\frac{1}{2}} = \sqrt{\frac{\rho_{s,i+1}}{\rho_{s,i}}} \tag{II.19}$$

$$\begin{aligned}\hat{\rho}_{s,i+\frac{1}{2}} &= S_{s,i+\frac{1}{2}}\rho_{s,i} \\ \hat{v}_{s,i+\frac{1}{2}} &= \frac{S_{s,i+\frac{1}{2}}v_{i+1} + v_i}{1 + S_{s,i+\frac{1}{2}}}\end{aligned} \tag{II.20}$$

$$h_t = h + \frac{1}{2}v^2 = c_pT + \frac{1}{2}v^2 \tag{II.21}$$

$$F_{i+1} - F_i = [\hat{L}][I\hat{\lambda}][\hat{R}](U_{i+1} - U_i) \tag{II.22}$$

Higher Order Godunov Method

The algorithm for solving the inviscid fluxes on which the IFE chamber code used in Reference [7] was built is a second order Godunov method. The technique used for the multi-species code follows that of Reference [7] closely. A basic explanation of the Godunov method for Euler equations can be found in Reference [15]. The Riemann solver implemented in the IFE chamber code is based the work of Colella in References [5] and [6].

To achieve higher order spacial accuracy, the algorithm uses slopes as developed in Reference [5]. The face states are calculated using a single step of the hybrid Glimm-Godunov approximate Riemann solver developed in the Appendix of Reference [6]. In particular, Equations II.23 and II.24 are used to determine the pressure and velocity between the $u \pm c$ sonic characteristics.

$$p^{*,0} = \frac{C_L p_R + C_R p_L + C_L C_R (u_L - u_R)}{C_L + C_R} \tag{II.23}$$

$$u^* = \frac{W_L u_L + W_R u_R + (p_L - p_R)}{W_L + W_R} \tag{II.24}$$

$$W_{L,R}(p^*) = C_{L,R}\sqrt{1 + \frac{\gamma + 1}{2\gamma}\frac{p^* - p_{L,R}}{p_{L,R}}} \tag{II.25}$$

$$C_{L,R} = \rho_{L,R} c_{L,R} = \sqrt{\gamma p_{L,R} \rho_{L,R}} \tag{II.26}$$

Unlike Roe's scheme, this approach correctly handles the case in which a the cell face lies within a rarefaction wave. Figure II.3 shows a view of the Riemann problem in such a configuration. In Roe's scheme, the rarefaction wave is just treated as another shock with an average velocity and sound speed.

The continuity and momentum equations appear identical to the original equations for the IFE chamber code. The continuity equation is uninfluenced by the multi-species formulation, and the momentum equation is only influenced

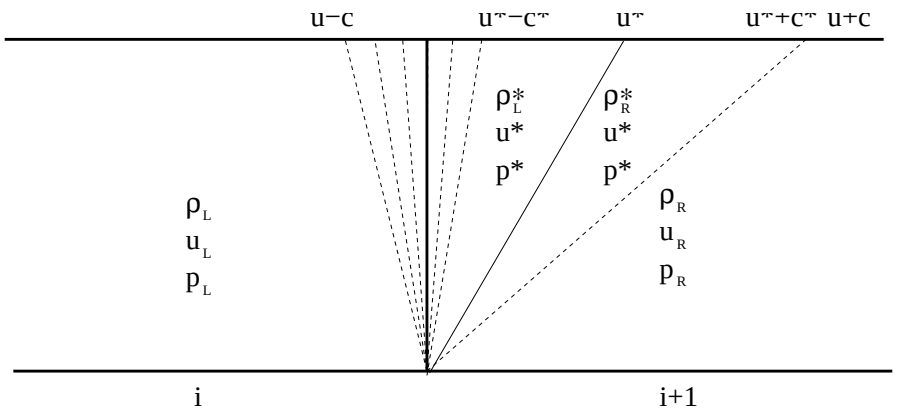

Figure II.3: Riemann problem with rarefaction wave

through the effect of composition on the transport coefficients. The energy equation has an added term due to the heat flux carried by the diffusion velocity. This extra heat flux is included with the advective heat flux.

The flux for the species conservation equations were calculated in an analogous manner to the continuity equation. As with the continuity equation, a predictor step is first used to estimate the state variables at time $t^n + \frac{1}{2}\Delta t$ at the cell centers. The multi-species algorithm includes the individual species densities in these estimates. The corrector step then uses the state at $t^n + \frac{1}{2}\Delta t$ to calculate the advective fluxes on the cell faces from time t^n to time t^{n+1} used to update the flowfield. However for the species conservation, the face state is determined by the sign of the bulk velocity plus the corresponding diffusion velocity rather than just the bulk velocity. This is the appropriate choice because the Riemann characteristic for the species conservation from the Jacobian of the flux is $v_0 + V_s$.

Once the state at the face has been determined, the fluxes are calculated as described in Equation II.2. The mass and bulk momentum flux terms are calculated as they were with the original IFE chamber code. The energy flux is first calculated exactly as in the original method, and then diffusion energy flux is added. Finally, the conservative species flux, $\rho_s(v_0 + V_s)$, is calculated using the cell face values as well as the cell centered left and right states when derivatives are needed.

II.B Transport Coefficients

For both numerical models, viscosity, thermal conductivity, thermal diffusion, and binary diffusion coefficients were calculated at each cell using temperature curve fits extracted from the preprocessor output of the Reactor Design's ChemKin software package. The ChemKin theory manual[18] gives further details of the techniques used which are closely related to the development from the theory section.

Xenon was not included in the basic chemical database of ChemKin. Though it was later discovered that ChemKin included another thermodynamic database with Xenon from the JANAF tables, the information needed to augment the basic chemical database provides insight into the information needed for the ChemKin preprocessor. The values for Xenon's Leonard-Jones potential were taken from Appendix Table I-A of Hirschfelder, Curtiss, and Bird [13]. The curve-fits for the thermodynamic data of Xenon came from NASA/TP-1999-208523 [10]. Though the JANAF data was valid on a larger temperature range, the thermodynamic data for Xenon was nearly identical from both the NASA and the JANAF data. Much more information about the ChemKin preprocessor inputs and outputs can be found in the ChemKin input manual[19].

The mixture average viscosity and thermal conductivity are produced using the curve fits for pure species viscosity and thermal conductivity and the semi-empirical Equations II.27 and II.29 from Reference [3] and [18]. This is a tradeoff of accuracy for significantly reduced computational complexity. In the validation section, comparison is made between these curve fit values and experimental data.

$$\mu = \sum_{s=1}^{S} \frac{X_s \mu_s}{\sum_{r=1}^{S} X_r \Phi_{sr}} \tag{II.27}$$

$$\Phi_{sr} = \frac{1}{\sqrt{8}} \left(1 + \frac{m_s}{m_r}\right)^{-\frac{1}{2}} \left[1 + \left(\frac{\mu_s}{\mu_r}\right)^{\frac{1}{2}} \left(\frac{m_r}{m_s}\right)^{\frac{1}{4}}\right]^2 \tag{II.28}$$

$$\lambda = \frac{1}{2}\left(\sum_{s=1}^{S} X_s\lambda_s + \frac{1}{\sum_{s=1}^{S} X_s\lambda_s}\right) \tag{II.29}$$

Equation I.14 requires the ordinary multicomponent species diffusion coefficients. Rather than solving Equation I.21 for these coefficients, the ChemKin manual defines a mixture average diffusion coefficient shown in Equation II.30 such that the diffusion velocity can be calculated using Equation II.31 instead of Equation I.14.

$$D_{sm} = \frac{1 - Y_s}{\sum_{r=1\ r\neq s}^{S} X_s/\mathcal{D}_{rs}} \tag{II.30}$$

$$V_{is} = -\frac{n}{n_s} D_{sm} d_{is} - \frac{D_s^T}{\rho_s}\frac{\partial lnT}{\partial x_i} \tag{II.31}$$

Though newer versions of ChemKin depend on full multi-species thermal diffusion coefficients as used in Equations I.14 and II.31, a simplified approximate method is also included for backwards compatibility. The simplified method uses Equation II.32 for the thermal diffusion term of the diffusion velocity where the thermal diffusion ratio, Θ_s, is of the form shown in Equation II.33. The thermal diffusion factor, $k_{sr}(t)$, is reduced to a curve fit dependent only on temperature. The formula given in Equation II.33 is an extension of the concept of the binary thermal diffusion ratio to multi-species applications. In the case of binary mixtures, it can be shown that Θ_s reduces to k_T as defined in Equation I.18. In this case, Equation II.32 is also equivalent to Equation I.14. When more species are considered, this method becomes an estimate for the thermal diffusion of a light species within a heavier mixture. For this reason, ChemKin only provides $k_{sr}(t)$ for species pairs with mass ratios greater than five.

$$V_{is} = -\frac{n}{n_s} D_{sm} d_{is} - \frac{D_{sm}\Theta_s}{X_s}\frac{\partial lnT}{\partial x_i} \tag{II.32}$$

$$\Theta_s = \sum_{r\neq s}^{S} k_{sr}(T) X_r X_s \tag{II.33}$$

Chapter III

Validation

The validation of the multi-species algorithm consists of two sections. In the first, comparison is made between experimental values and numerical estimates for the composition dependence of the transport coefficients. The second section shows the effect of the diffusion velocities on the shape of shock waves.

III.A Transport Coefficients

Comparison is made between tabulated experimental data and numerical estimates for viscosity and thermal conductivity across the range of compositions for Helium-Xenon gas mixtures. Experimental values for these coefficients were tabulated in Reference [23]. Thermal diffusion ratios are also compared to values from Reference [1]. Finally in Table III.A, the binary diffusion coefficients for the He:Xe system from the application are compared to analytical and experimental values.

The largest discrepancy appears in the thermal diffusion ratio. Because $k_{sr}(t)$ is independent of composition, the equation necessarily produces parabolic thermal diffusion ratios when plotted against number fraction. Reference [1] also includes experimental data for Xe:Ar thermal diffusion ratios that are closer to parabolic suggesting that the asymmetry may be a result of the large Xe:He mass ratio. The ChemKin theory manual mentions that this method of calculating ther-

Table III.1: Reference and Application Binary Diffusion Coefficients at 1 Atm

Gas Pair	T(K)	Analytical $\mathcal{D}, (cm^2/s)$	Experimental $\mathcal{D}$	Application $\mathcal{D}$
He:He	300	1.700 [14]		1.681
He:Xe	303	0.604 [21]	0.600 [21]	0.540
Xe:Xe	300.5	0.0571 [13]	0.0576 ± 0.0009 [13]	0.05594

mal diffusion is considerably less accurate than the full multicomponent method now used in their application, but due to the complexity and expense of the full multicomponent method, this approximation is used to provide initial indication of the importance of including thermal diffusion in the IFE target application.

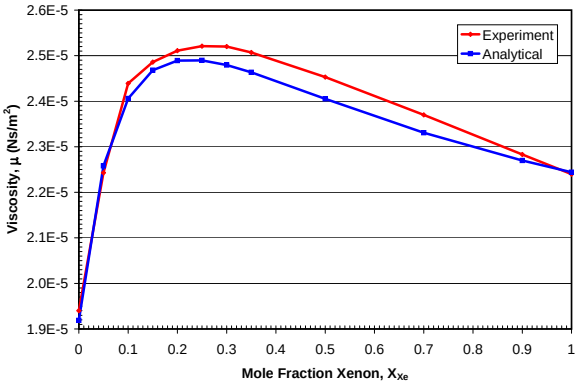

Figure III.1: Viscosity by Composition for He:Xe Mixture

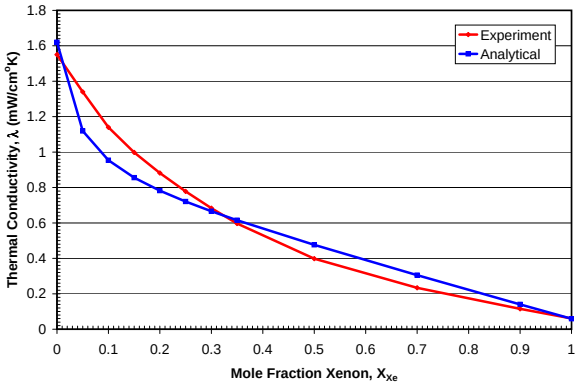

Figure III.2: Thermal Conductivity by Composition for He:Xe Mixture

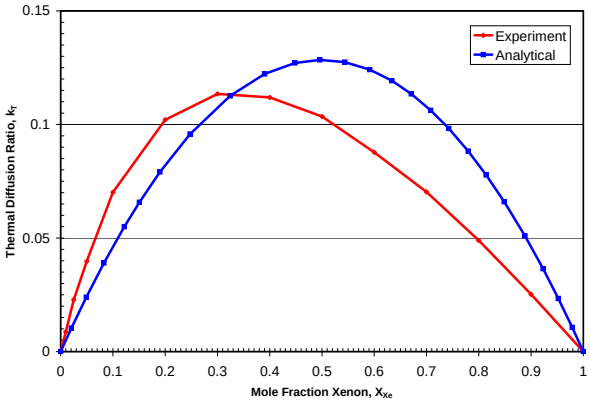

Figure III.3: Thermal Diffusion Ratio by Composition for He:Xe Mixture

III.B Shock Broadening

In order to validate the numerical methods, comparison is made between experimental and simulation data for the composition dependence across a shockwave for a mixture of noble gasses. The experimental data available shows the shock broadening and mixture separation for a mixture Helium and Xenon gas at two different Mach numbers.

The reason that the composition varies across the shockwave is inherently due to the Dufour and Soret effects. Though typically the Soret effect is considered with respect to instability in buoyancy driven flows, the tendency for lighter gasses to diffuse up temperature gradients is present within the shock as well. The strong temperature and pressure gradients within the shock drive these phenomena to actually work against the standard Fickian diffusion term and cause the gas to become less uniformly mixed. Because the energy is partitioned equally between the Helium and Xenon atoms, the Helium atoms move on average $\sqrt{m_{Xe}/m_{He}}$ faster. This results in Helium atoms crossing the discontinuity from further upstream. The Xenon atoms also have more momentum and therefore take longer for their directional pre-shock velocity to randomize into thermal noise. The multispecies formulation is capable of capturing the continuum representation of some of these effects as long as the gasses do not deviate far from equilibrium distribution functions.

III.B.1 Study Conditions

The experimental values were obtained from the work of Herczynski, Tarczynski, and Walenta[12]. These experiments were performed in a shock tube using an electron gun and laser differential interferometer to measure the composition across the shock. The experiments were performed with Helium-Xenon gas mixtures with percent composition by number fraction rather than by mass fraction. At 3% Xenon number fraction, the mass fraction is approximately 50% Xenon and

50% Helium.

One and two-dimensional multi-species Navier Stokes codes based on the development in the previous sections were used to simulate the shock structure for the conditions in Reference [12]. The simulation results are shown in Figures III.4 and III.5 for Mach 1.54 and Mach 4.38 respectively. In the figures, the flow is from left to right across the shock.

The simulation length scale results were nondimensionalized using the mean free paths listed in Reference [12]. The densities were normalized according to Equation III.1 as was the data in Reference [12]. In the equation, L and R subscripts refer to the state at the left and right edge of the numerical domain respectively. The discrepancy between the numerical and experimental value near the start and end of Figure III.4 might be an artifact due to this normalization. The experiment may have defined the left and right states based on the apparent start and end of the shock rather than the states further up and downstream.

The one-dimensional implementation was incorporated into the existing algorithm for the two-dimensional explicit time-stepping compressible code used for IFE chamber gas simulation. Because this code uses a spatially split flux calculation, adding the effects of the multi-species diffusion consisted of simply calculating the diffusion velocities and corresponding fluxes on the cell faces for both directions. The curves plotted from the 2D codes were extracted from the centerline of the computational domain parallel to the flow.

As seen in Figures III.4 and III.5, the resulting shock composition agree well between the one and two-dimensional version. Both the one and two-dimensional codes showed better agreement to experimental data for the Mach 1.54 case than for the Mach 4.38 case. This result is not unexpected and explained in further detail in the following section.

$$\hat{\rho} = \frac{\rho - \rho_L}{\rho_R - \rho_L} \tag{III.1}$$

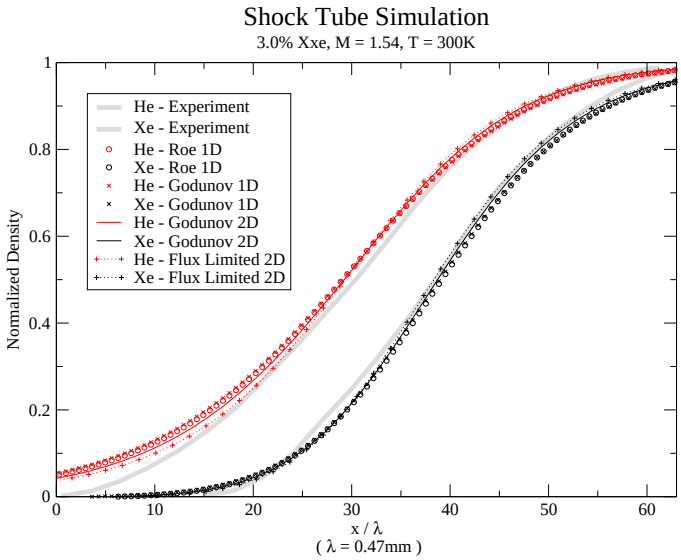

Figure III.4: Shock broadening simulation results and experimental data, Mach 1.54.

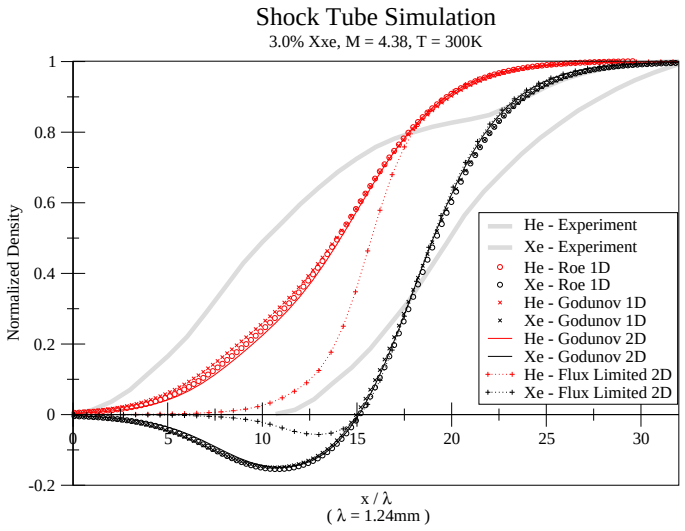

Figure III.5: Shock broadening simulation results and experimental data, Mach 4.38.

III.B.2 Strengths and limitations

As discussed in Chapter 10 of Vincenti and Kruger [24], because the Navier-Stokes equations are fundamentally based on a an expansion around equilibrium, their results are expected to deviate from experimental values for strong shock-waves. For this reason, Reference [24] mentions methods that try to account for non-equilibrium distribution functions such as Mott-Smith and BGK for estimating shock thickness of stronger shocks. However, comparisons with experimental data suggest Navier-Stokes performs better than what would be expected from a purely theoretical standpoint.

III.B.3 Shockwave Comparison

As seen in Figure III.4, all the simulations including the flux limited case match the experimental data and each other at Mach 1.54 quite well. Figure III.5 shows that the simulation starts to capture some of the general trends such as shock width and composition separation for the strong shock. The simulations fail to capture the internal structure of the strong shock-wave such as the "hump" in the shock-wave.

Along with the experimental data, a theoretical model was included in Herczynski, Tarczynski,and Walenta[12]. Their model used a variational model to approximate the Boltzmann equation directly. They captured the "hump" in the shock-wave, but their model resulted in no separation at the beginning of the shock-wave along with quantitatively inaccurate shock composition and width values. Their theoretical model showed a large temperature overshoot in the heavy component of the mixture near the hump.

The Navier-Stokes type derivation used in the simulations of this paper depends on nearly instantaneous energy relaxation between the components because the distribution functions are assumed to be perturbations to the Maxwellian distribution when the Chapman-Enskog expansion is performed. The simulations therefore necessarily cannot capture a temperature overshoot in one component

because the instantaneous energy relaxation corresponds to equal temperatures for all the components. This most likely explains the lack of a "hump" in the simulations. Unfortunately, Herczynski, Tarczynski, and Walenta were unable to generated a temperature profile experimentally to confirm the overshoot.

At the Mach 4.38, the simulations predict that the heavier component accelerates at the beginning of the shock producing a drop in the density that is not found in the experimental data. This effect was also found by Sherman [20] using a completely different numerical method for solving the multi-species Navier-Stokes equations.

The Mott-Smith and BGK models were developed in an attempt to calculate the shape of strong shock-waves more accurately. The BGK model predicts a velocity drop that begins much further upstream from the shock-wave[24]. If the BGK profile was the underlying shape instead of the Navier-Stokes solution, this early deceleration of the profile would help the simulation match the experimental data better. Unfortunately, the BGK model employs an iterative solution to a set of integro-differential equations and would be much more difficult to extend to multiple dimensions

The flux limited Mach 4.38 case differs significantly from the other Mach 4.38 cases. In particular, the flux limited case reduces the early acceleration of the heavier component. This suggests that the cause of this fictitious acceleration is likely the result of diffusion velocities unrealistically large for the theoretical model. The Xenon acceleration may actually result from the requirement that the weighted sum of diffusion velocities be zero in this formulation.

For the intended application of IFE chamber gas simulation, the internal structure of very strong shocks is not of great importance. These simulations are primarily intended to indicate that the addition of the multi-species effects are properly calibrated and to indicate the mechanism through which the formulation breaks down. Features such as broadened shock width and the ability to track the effects of composition on transport coefficients are more relevant. The results

indicate that applying the multi-species continuum model to fluid structures on the scale of tens of mean free paths is not unreasonable for situations in which the fluid remains close to local equilibrium. A more robust treatment of other non-equilibrium effects such as ionization and radiation are much more likely to effect results than extension to accurately reflect strong shock structure.

Chapter IV

Application

IV.A IFE Chamber Gas

Viable Inertial Fusion Energy (IFE) power production requires the efficient absorption of short and intense energy pulses in rapid succession within the reaction chamber. Between target injections, trace chamber gas is used as a buffer to absorb and reradiate these intense energy bursts to limit the peak impulse on the chamber walls. However, this chamber gas must relax to conditions that allow for target survival during subsequent injections.

Figure IV.1 shows the volume averaged temperature for a typical potential IFE chamber design. The volume average for temperature is defined in the "Cold Jets" subsection. For this and the remaining cases, a simple $10m$ radius axisymmetric half height cylinder was used as the numerical domain. The radiation hydrodynamics code "BUCKY" was used for the target implosion to produce the initial conditions for the fluid code because the fluid code does not have the capability to perform the fusion burn calculations. As mentioned in the continuum approximation section, "BUCKY" used an initial chamber density corresponding to 50 milli-torr pressure at room temperature. All times stated are based on the fluid code's clock starting at the end of the "BUCKY" case used as initial conditions. The time from "BUCKY" for the initial conditions is an additional $0.5ms$.

Further details of the equivalent baseline case can be seen in the work Dragojlovic and Najmabadi in Reference [9].

Despite a rapid temperature drop for the first few milliseconds, from approximately 10-100ms the chamber temperature remains relatively constant at approximately 3000K. Though the majority of the energy is radiated to the walls, techniques for quickly reducing the remaining gas temperature could increase the overall system efficiency. Such techniques could also potentially lessen chamber vacuum requirements. Lower vacuum requirements would thereby reduce vacuum pumping complexity and expense and also reduce the peak instantaneous heat flux on the walls.

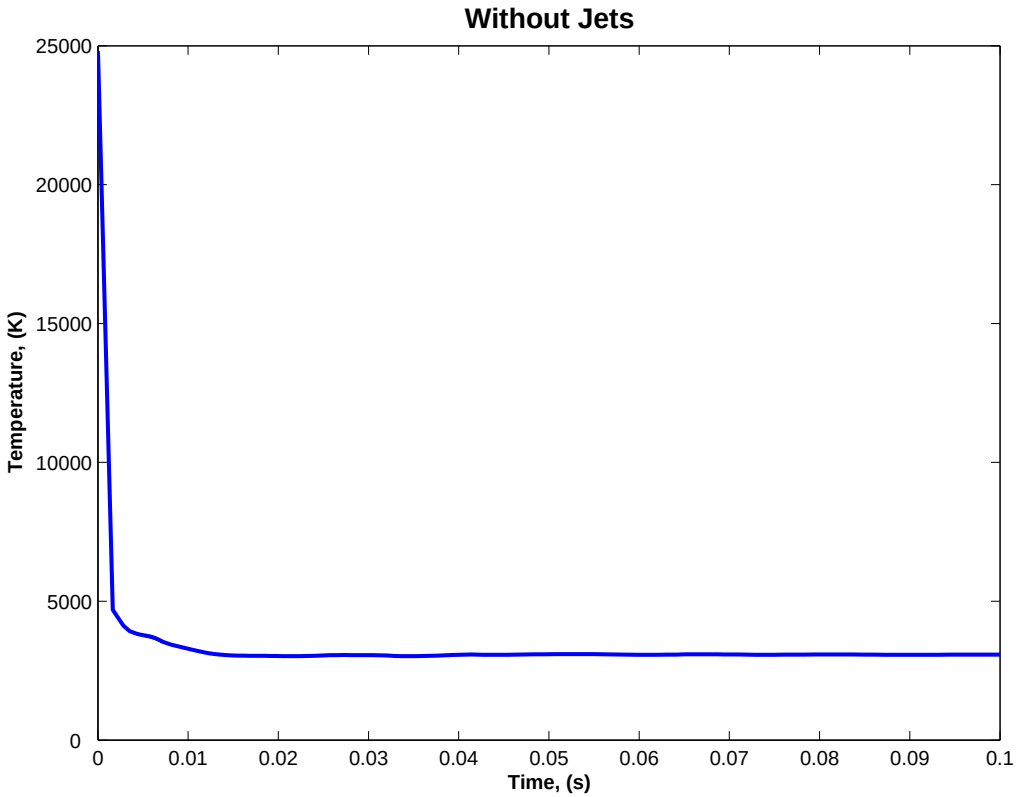

Figure IV.1: IFE chamber temperature without cold jets

IV.A.1 Cold Jets

The potential of using cold gas jets to enhance mixing and to lower the average chamber temperature is investigated in this section. Because the temperature could be reduced to an arbitrarily low level with a large enough cold gas input, the relative level of mixing for various configurations is of greater importance. Along with a zero jet control, cases were run with one to three jets included on the top and side walls of the numerical domain. Three different jet densities were also investigated for each set of jets. In all the cases, the temperature and velocity of the jet inlet were set to the choke conditions for a room temperature gas isentropically accelerated to Mach 1.

The temperature change is based on Equation IV.1 for choked flow from Reference [2] resulting in a jet temperature of 223.5 K down from 298 K. In the equation, T_0 is the reservoir temperature and T^* is the choked temperature. The temperature then sets the sound speed. A mass flux sufficient to result in final temperatures similar to the wall temperature of 973 K was then selected. A jet pressure was also selected to ensure that jet remained sonic into the chamber at peak chamber gas pressure on the wall. This specified the jet density and finally jet width. Three other lower jet pressures were then selected based on densities of 2/3 and 4/9 the original density.

Three different jet configurations were then selected. The position of the jet centers are shown in Figure IV.2. The width of the jets were selected so that the total energy and mass injected into the system would be approximately equal for all the cases. For all the cases, the jets were started at $10ms$ and stopped at $20ms$. The chamber gas was then allowed to evolve until $100ms$.

$$\frac{T^*}{T_0} = \frac{2}{\gamma + 1} \tag{IV.1}$$

It is important to note that the extent to which such a system could be implemented depends on the vacuum pumping capacity. Injecting gas into the chamber requires a pressure gradient such that the total chamber pressure and

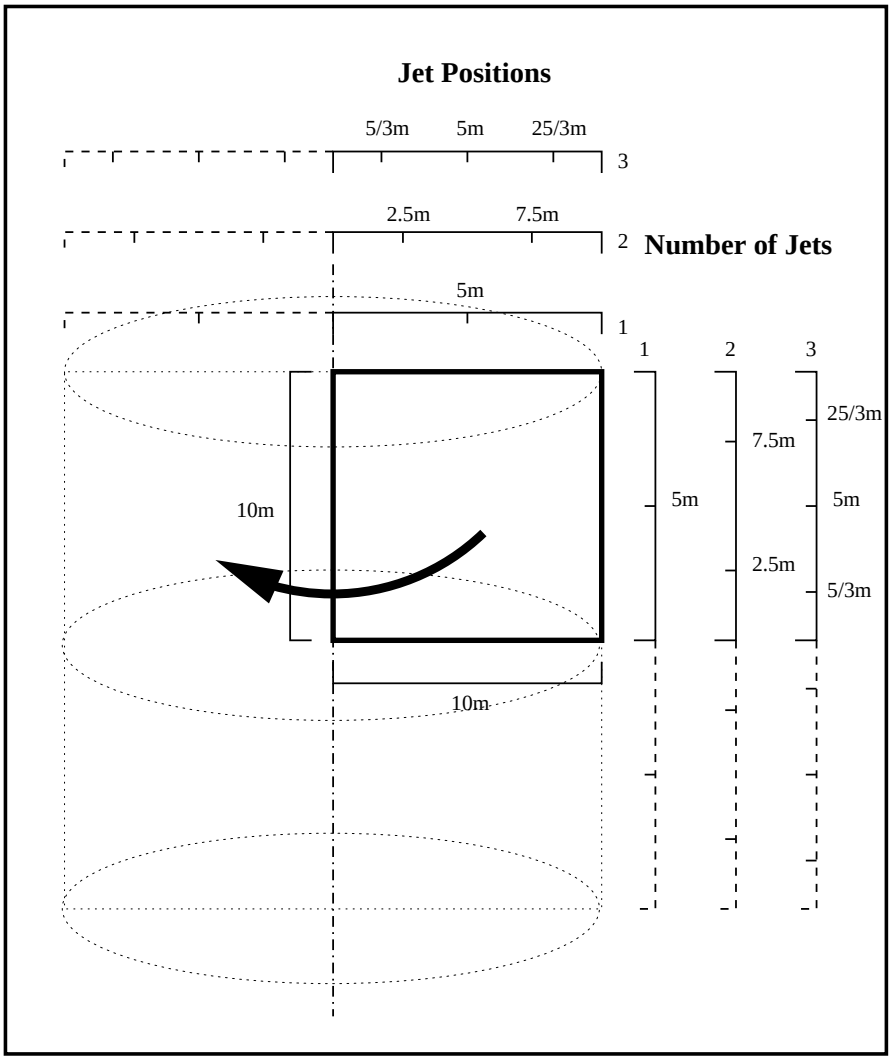

Figure IV.2: IFE Chamber Jet Configuration

energy density are increased. Though the chamber gas temperature is decreased, it is at the expense of the vacuum. Whether the chamber gas energy density or temperature is more relevant to target survival depends on whether the heat flux to the target is dominated by radiative or fluid mechanical processes. Further details on target survivability can be found in Reference [4]. However, inclusion of these jets could only be implemented in steady state with a corresponding increase in vacuum pumping capacity. Though the effects of vacuum pumping capacity were beyond the scope of this study, it is assumed that the vacuum and jet systems would be designed to compensate for the increased pressure and hence energy density due to the jets, should such a system be implemented. For this reason, the final chamber gas temperature was selected to be of primary interest.

In order to quantify the extent to which the jets thermally mix with the pre-existing chamber gas, comparison was made between the mass averaged and volume averaged temperatures. If the two gasses are completely mixed, the mass and volume averaged temperatures should be the same. If not, the hot low density gas that was originally in the chamber should be over-represented in the volume average. Equations IV.2 and IV.5 show how the mass and volume average temperatures respectively are calculated. Equation IV.6 gives an expression used for the normalized thermal mixing residual. In this equation, zero corresponds to perfect mixing.

$$T_m = \frac{\iiint_\Gamma \rho[e_{int}] r dr dz d\theta}{\bar{c}_v \iiint_\Gamma \rho r dr dz d\theta} \tag{IV.2}$$

$$\bar{c}_v = \frac{3}{2}\frac{R}{\bar{m}} \tag{IV.3}$$

$$\bar{m} = \frac{\sum_{s=1}^{S} m_s \iiint_\Gamma n_s r dr dz d\theta}{\iiint_\Gamma n\, r dr dz d\theta} \tag{IV.4}$$

$$T_v = \frac{\iiint_\Gamma [e_{int}/c_v] r dr dz d\theta}{\iiint_\Gamma r dr dz d\theta} \tag{IV.5}$$

Table IV.1: Normalized thermal mixing residual across range of jet number and density

η_T	1 Jet	2 Jets	3 Jets
ρ_0	1.054	0.559	0.359
$2/3\rho_0$	1.052	0.558	0.412
$4/9\rho_0$	0.910	0.619	0.472

$$\eta_T = \frac{T_v - T_m}{T_m} \tag{IV.6}$$

Table IV.A.1 shows the the normalized thermal mixing residual for the nine different jet cases.

In general, the thermal mixing residual is decreased with more smaller higher density jets. Though the temperature and therefore choked velocity is the same for all of the cases, the higher density jets correspond to higher pressure. This causes the higher density jet gas to accelerate supersonically and cool upon entering the target chamber. This also results in more vigorous mixing of the hot and cold gasses within the chamber. The only discrepancy from the trend of denser jets corresponding to better thermal mixing is found in the lowest density one jet case. This is likely due to overall delayed mixing due to the large jet size in all of the one jet cases.

Figure IV.3 shows the time history of the difference between the volume average temperatures for the medium and low density cases, denoted T_2 and T_3, compared to the high density case, denoted T_1, for each number of jets. Values below zero correspond to volume average temperatures below those of the highest density case. The figure shows that for all the cases, lower density jets initially produce cooler volume averaged temperatures than their higher density counterparts. This is reasonable because the lower density cases have wider choke points to accommodate the same mass and energy fluxes. This results in a larger volume of low temperature jet gas as it enters the chamber. However later on in the sim-

ulation, the enhanced mixing reverses this original trend. Because the jets in the one jet cases are so large, this reversal has not yet occurred in the simulation time interval.

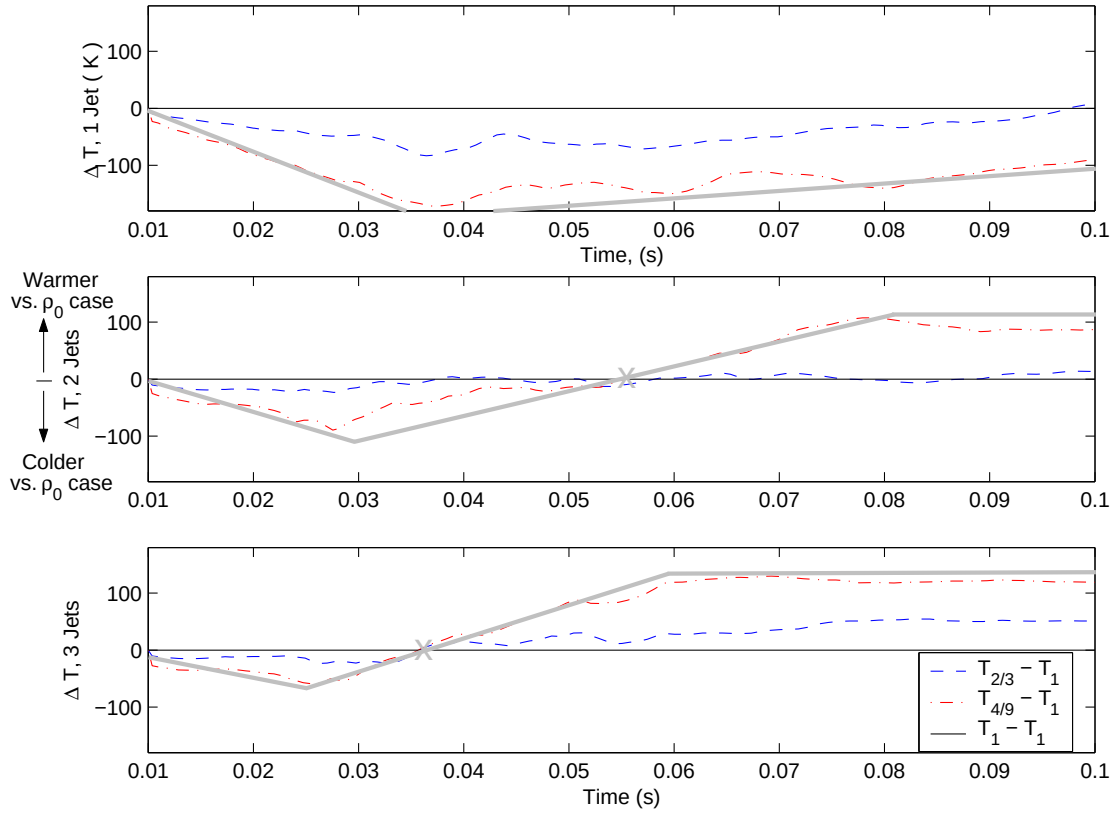

Figure IV.3: Time history of volume average temperature difference for medium and low density jets versus high density jets. The gray lines highlight the general trends discussed in the text.

Total and local volume averaged jet mass fraction was also calculated to help quantify physical mixing. Equations IV.7 and IV.8 show the corresponding equations. These quantities should also be equal if the jet gas is completely mixed with the chamber gas. This results in Equation IV.9 for the normalized physical mixing residual. Table IV.A.1 shows the corresponding final normalized physical

Table IV.2: Normalized physical mixing residual across range of jet number and density

η_Y	1 Jet	2 Jets	3 Jets
ρ_0	0.25	0.126	0.079
$2/3\rho_0$	0.26	0.125	0.093
$4/9\rho_0$	0.24	0.148	0.116

mixing residuals. Again, zero would correspond to a complete mixing.

$$\bar{Y_t} = \frac{\iiint_\Gamma \rho_{jet} r dr dz d\theta}{\iiint_\Gamma \rho r dr dz d\theta} \tag{IV.7}$$

$$\bar{Y_v} = \iiint_\Gamma \frac{\rho_{jet}}{\rho} r dr dz d\theta \tag{IV.8}$$

$$\eta_Y = \frac{\bar{Y_t} - \bar{Y_v}}{\bar{Y_t}} \tag{IV.9}$$

In the case of physical mixing, the trend of more jets promoting better mixing is again present, but higher pressure does not seem to promote better mixing. This is likely a result of relatively rapid thermal diffusion. Because the particles can exchange energy during a collision, the energy diffuses faster than the time it takes for the particles to randomly walk.

Figures IV.4 and IV.5 show the time histories of the jet mass fractions either by number of jets or jet density. In the figures, the upper lines correspond to the composition for a uniformly mixed chamber. This shows that despite slightly different mass fluxes due to numerical cell geometry, the average composition is nearly identical for the nine cases. The spaces between the upper and lower curves correspond to the deviation from uniform composition.

Comparing Figures IV.4 and IV.5 demonstrates the dramatically stronger contribution of number of jets than jet density to the final chamber composition. In Figure IV.4, each of the plots contain composition curves for different density jets with the same number of jets for each plot. In this figure, the three different

density composition curves nearly completely overlap. Figure IV.5 has the same data with the curves grouped by jet density instead of number of jets. This again shows that the number of jets plays a considerably larger role than jet density for physical mixing.

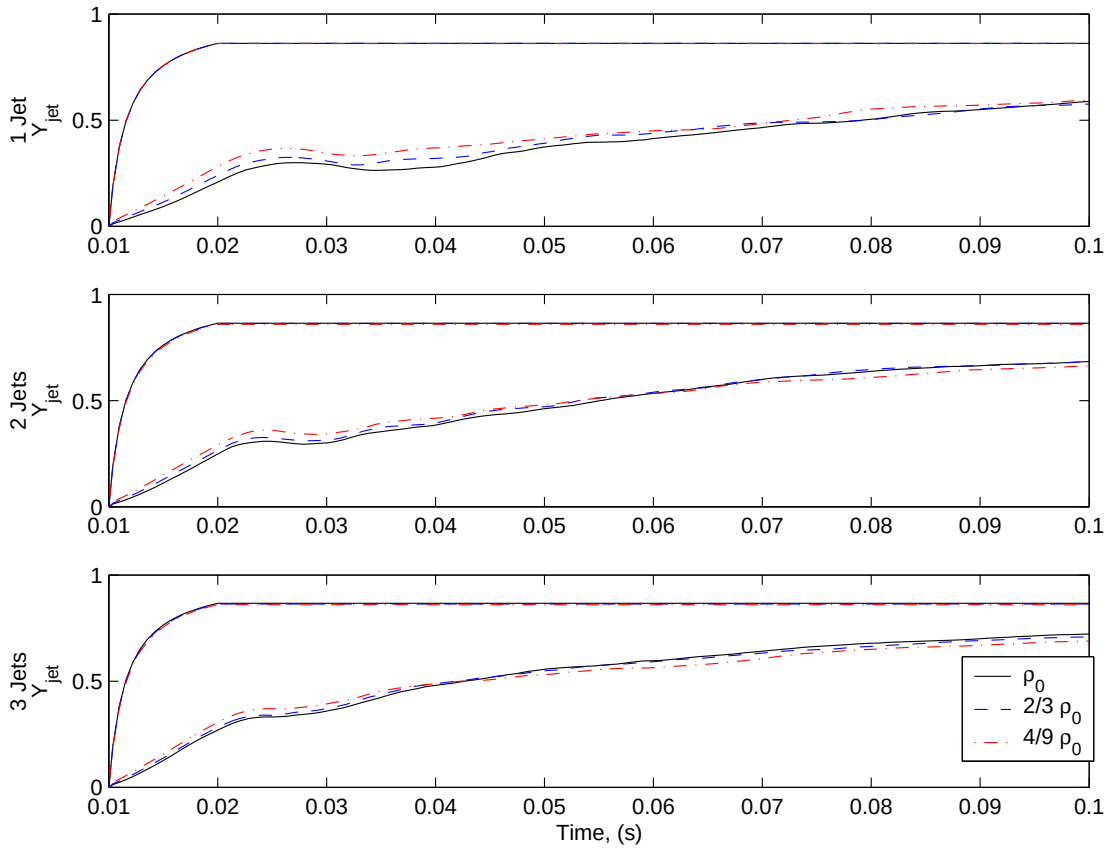

Figure IV.4: Time history of jet mass fraction by number of jets. Upper curves are total and lower curves are volume averaged.

It is interesting to note the slight decrease in volume average jet mass fraction slightly after the jet has been turned off. It is particularly apparent from approximately 25-45ms in the 1 jet cases. This is most likely caused by the collision of jets from the top and side. As the jets collide, the density of the gas increases resulting in lower volume averaged jet mass fractions despite the mixing occurring on the edges of the plumes. Figure IV.6 shows the gas densities immediately before

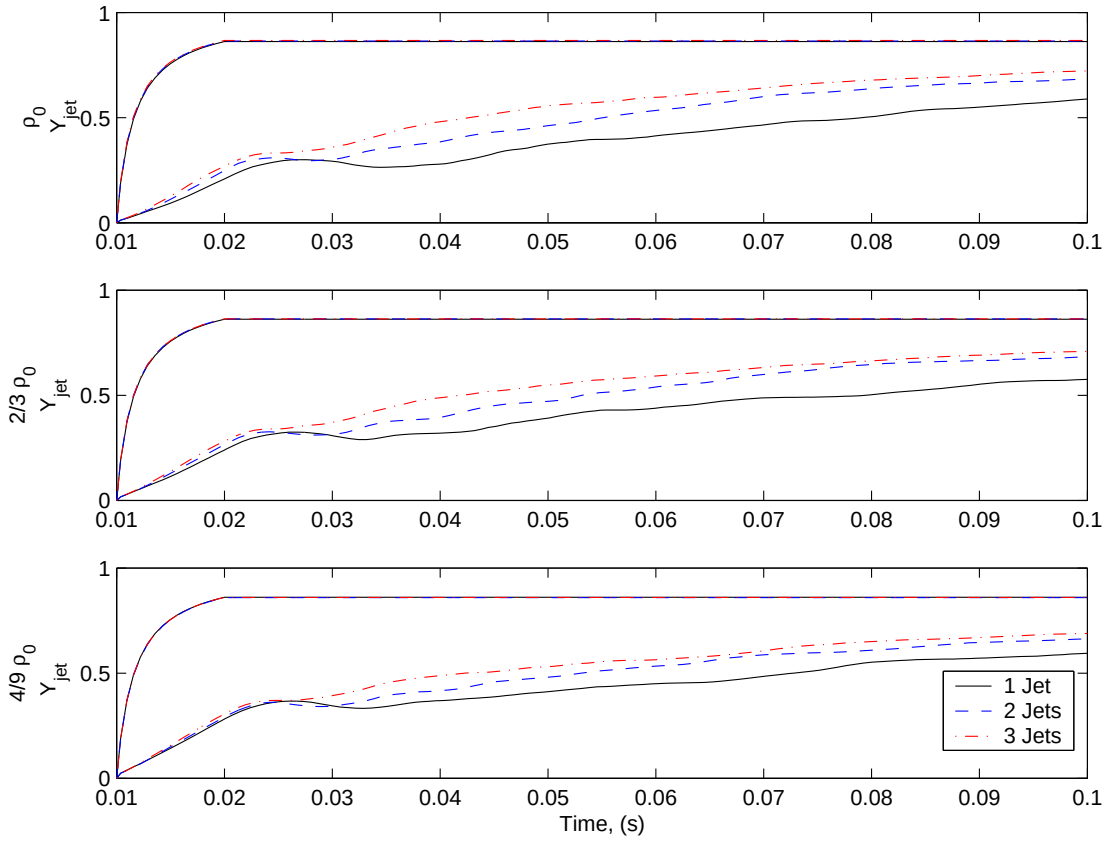

Figure IV.5: Time history of jet mass fraction by jet density. Upper curves are total and lower curves are volume averaged.

and during the collisions for the one jet high density case.

Based on the maximum compression of the jets colliding at $35ms$, or $15ms$ after the jets are turned off, for the 1 jet high density case, the 2 and 3 jet cases would be expected to reach maximum compression at around $27.5ms$ and $25ms$ respectively due to the chamber geometry. These estimates correspond well to local minimums seen in Figure IV.4. Though the 3 jet case appears to only have an inflection point at $25ms$, the mass fraction does in fact decrease approximately 0.01% before continuing upward. It is also not unexpected that the decrease would be more minor with the 3 jet cases simply because only a third of the total jet mass is involved in the collision at that time.

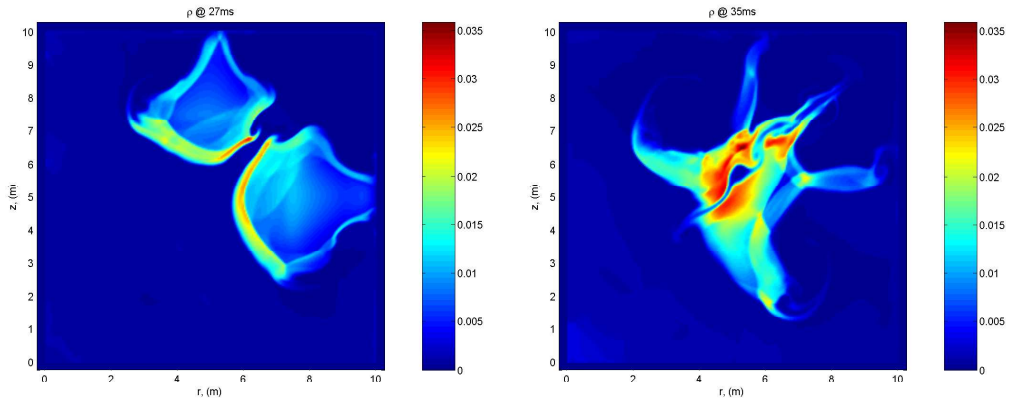

Figure IV.6: Density before and during jet collision for one high density jet case.

IV.A.2 He:Xe mixed jets

Injecting cold Helium-Xenon mixtures instead of pure cold Xenon is another way to decrease chamber equilibration time. Including Helium not only increases mixture average sound speed and thermal conductivity, but Helium will also thermally diffuse up temperature gradients in Helium-Xenon mixtures due to the "normal" Soret effect [11]. The energy of the hot gas is then partitioned between more particles further facilitating thermal equilibration.

All of the mixed jet cases are initially based on the "ρ_0" pure Xenon

3 jet configuration because it provided the best results from the cold jet cases. Table IV.A.2 shows the jet compositions required for the specified sound speed increase for the set of mixture cases run. The jet port width was also divided by the sound speed increase so that the mass or energy fluxes would match those of the pure Xenon case. Tables IV.A.2 and IV.4 show the properties for the six mixture cases run when compared to the three jet original density pure Xenon case that produced the best mixing of the pure Xenon cases. Jet mass and energy were normalized using the mass of the chamber gas and the total energy in the chamber at $10ms$ when the jets were started. As with the pure Xenon cases, all jets used a temperature of $223.5K$ and choke conditions. Tables IV.A.2 and IV.4 also show the final mass and volume averaged temperatures.

Figure IV.8 shows the evolution of composition for a typical mixed jet case at $20ms$ intervals. Figure IV.7 shows the corresponding evolution of the pure Xenon jet case. The plots in Figure IV.8 correspond to the energy flux matched case with jet gas sound speed at 150% that of the pure Xenon case. The first indication of thermal diffusion is seen in the $20ms$ plots as an orange smudge around the jet structures when compared to the sharp boundary of the pure Xenon case. As the jet Helium differentially diffuses into the hot chamber Xenon, areas of brighter green are eventually visible around the jet fluid structures. In general, the pure Xenon case maintains much sharper boundaries between the jet and chamber gases resulting in stripes as the gases twist around each other. The other obvious difference between the two cases is the difference between how far the jets have propagated into the chamber at $20ms$ due to the sound speed difference.

Figures IV.9 and IV.10 compare the composition of the six mixture cases at $20ms$ and $100ms$ respectively. They use the same color scale for number fraction as in Figures IV.8 and IV.7. In the figures, the energy flux matched cases are on the left while the mass flux matched cases are on the right. In the $20ms$ figure, the reduction of jet mass for the energy flux matched cases is particularly obvious for the 200% Xenon sound speed cases. For the energy flux matched cases, the higher

Table IV.3: He:Xe Jet Mixture Properties

Sound Speed	125%	150%	200%
$\bar{M}/M_{Xe}$	0.64	0.444	0.25
X_{Xe}	0.63	0.43	0.23
Y_{Xe}	0.982	0.961	0.906

Table IV.4: Fixed Mass He:Xe Jet Cases versus Baseline Cases

Fixed Variable	None	Both	Mass	Mass	Mass
Sound Speed	-	100%	125%	150%	200%
$\Delta M_j/M_c$	0.00	6.48	6.33	6.50	6.39
$\Delta E_j/E_{c,t=10ms}$	0.00	0.59	0.90	1.33	2.32
$T_{f,m}(K)$	2987	745	616	550	505
$T_{f,v}(K)$	3074	1013	955	641	539

Table IV.5: Fixed Energy He:Xe Jet Cases versus Baseline Cases

Fixed Variable	None	Both	Energy	Energy	Energy
Sound Speed	-	100%	125%	150%	200%
$\Delta M_j/M_c$	0.00	6.48	4.05	2.89	1.60
$\Delta E_j/E_{c,t=10ms}$	0.00	0.59	0.57	0.59	0.58
$T_{f,m}(K)$	2987	745	760	788	789
$T_{f,v}(K)$	3074	1013	1174	896	826

sound speeds correspond to further penetration into the chamber gas, but also a narrowing of the jets. For the $100ms$ figure, the plots show that the energy flux matched cases leave a region of bright red pure chamber Xenon whereas the mass flux matched cases appear to be completely mixed. The increase in jet energy in these cases enable the gas mixing to reach completion.

Table IV.A.2 shows the normalized thermal mixing residual for the mixed jet cases as defined for the pure jets. It is interesting to note that the residual is higher than the pure Xenon case for sound speeds of 125% that of pure Xenon. This is the result of a reduction in final mass average temperature more than an increase in final volume average temperature.

Only the energy fixed case at 125% sound speed ended with a higher

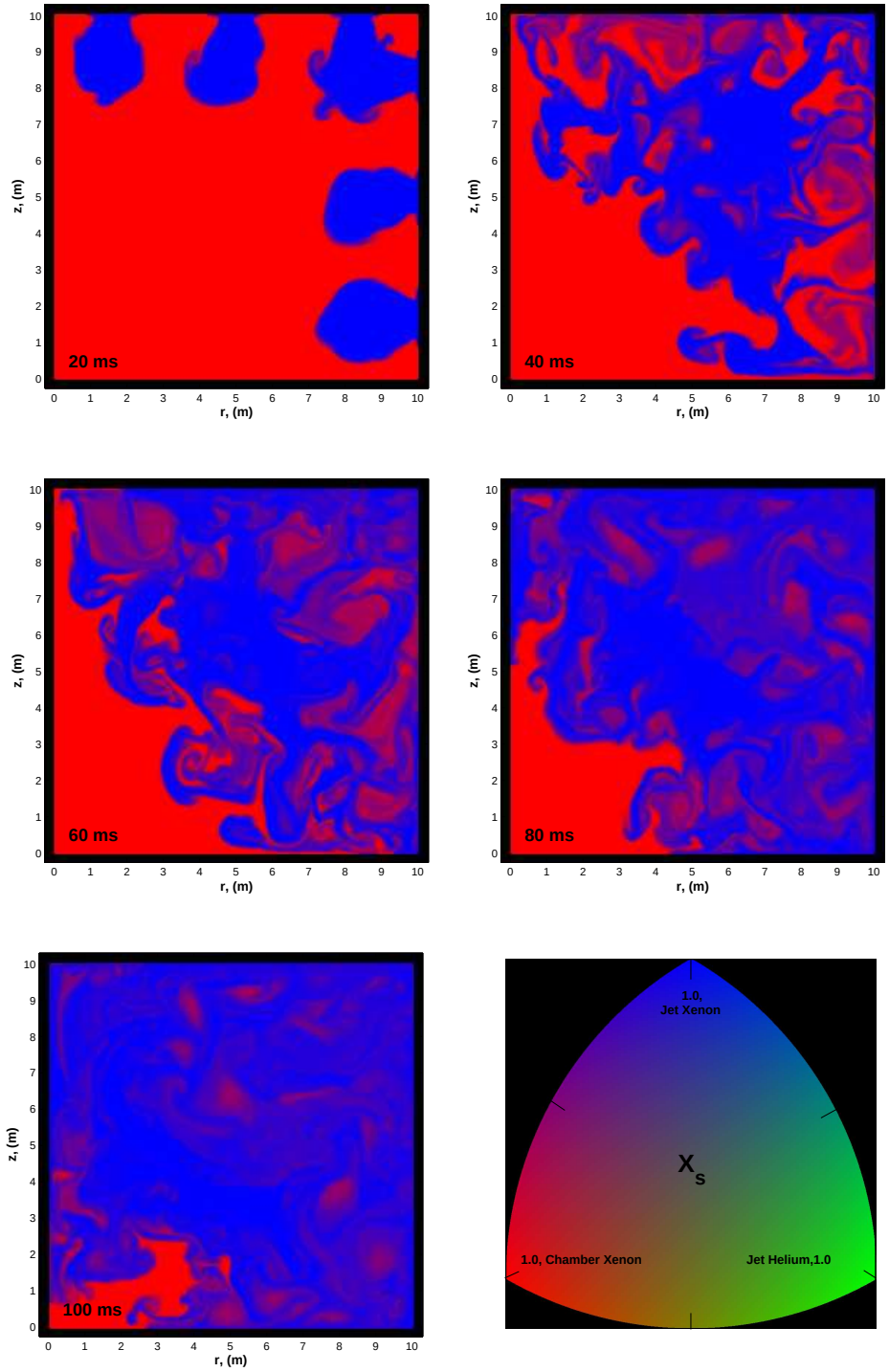

Figure IV.7: Mixture Number Fractions, Pure Xenon Jet Case

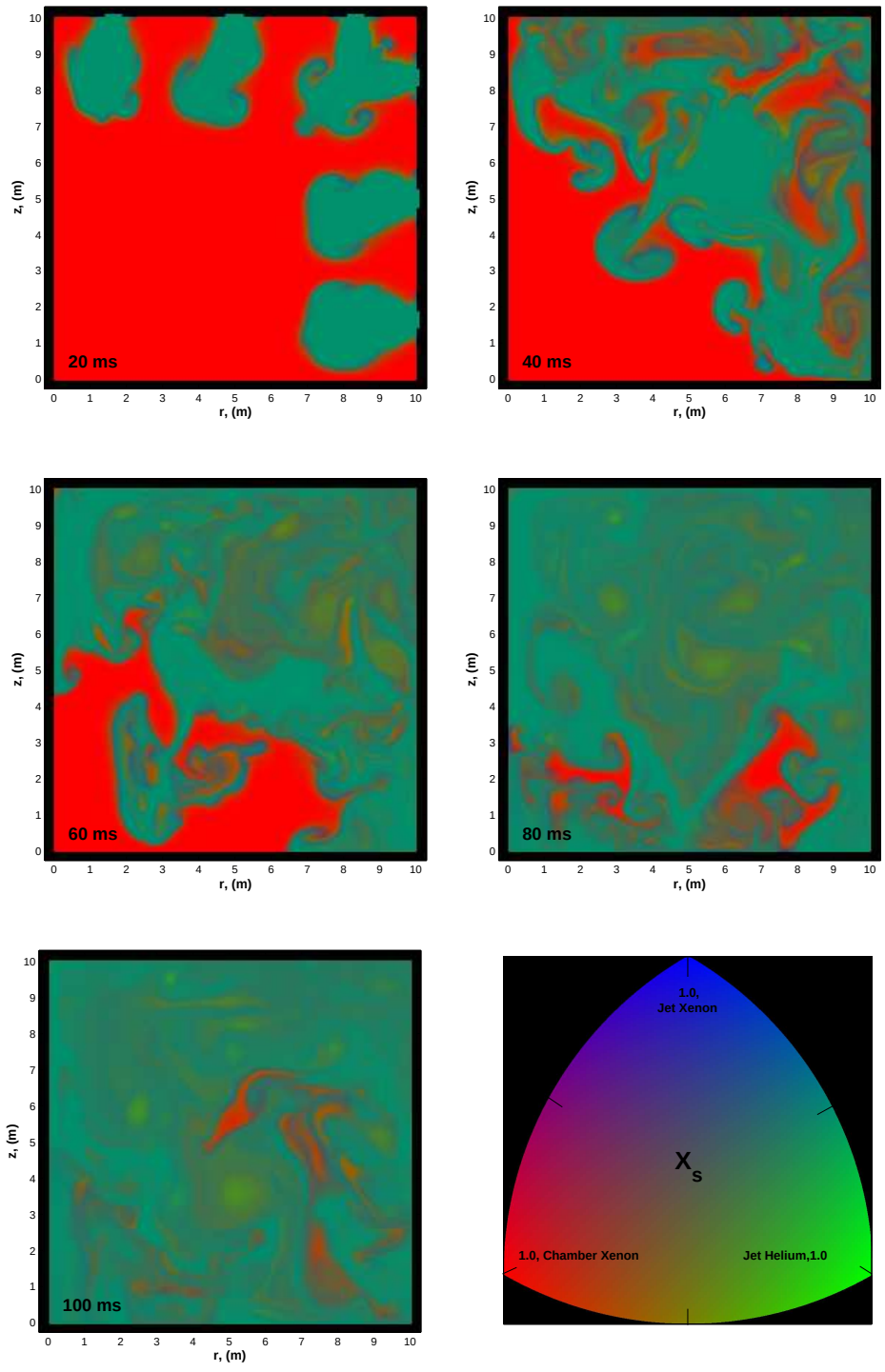

Figure IV.8: Mixture Number Fractions, 150% Xenon Sound Speed Jets, Energy Flux Matched to Xenon Cases

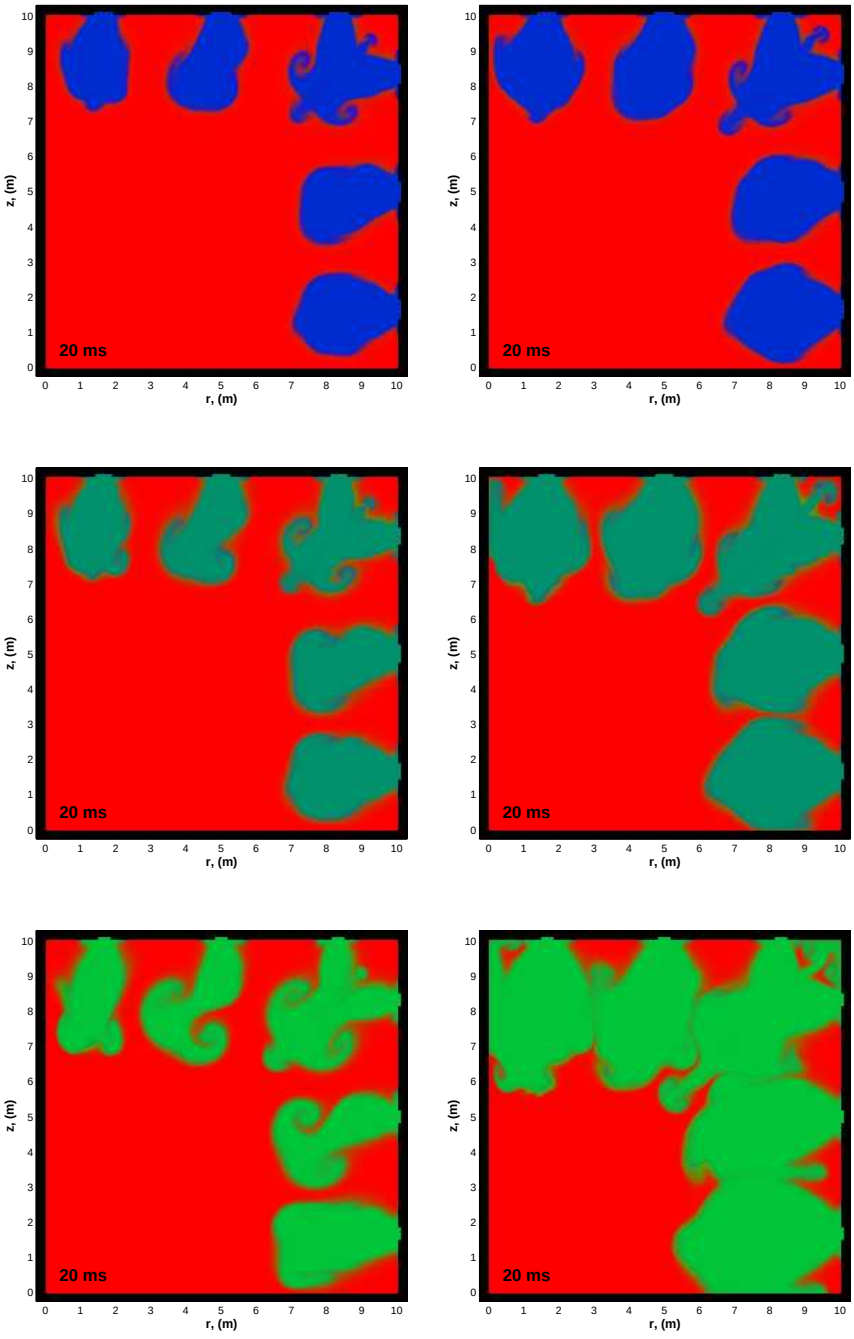

Figure IV.9: Mixture number fractions at $20ms$ for energy and mass flux matched cases. The left column corresponds to energy flux matched and the right column corresponds to mass flux matched. The rows are 125%, 150%, and 200% pure Xenon sound speed from top to bottom.

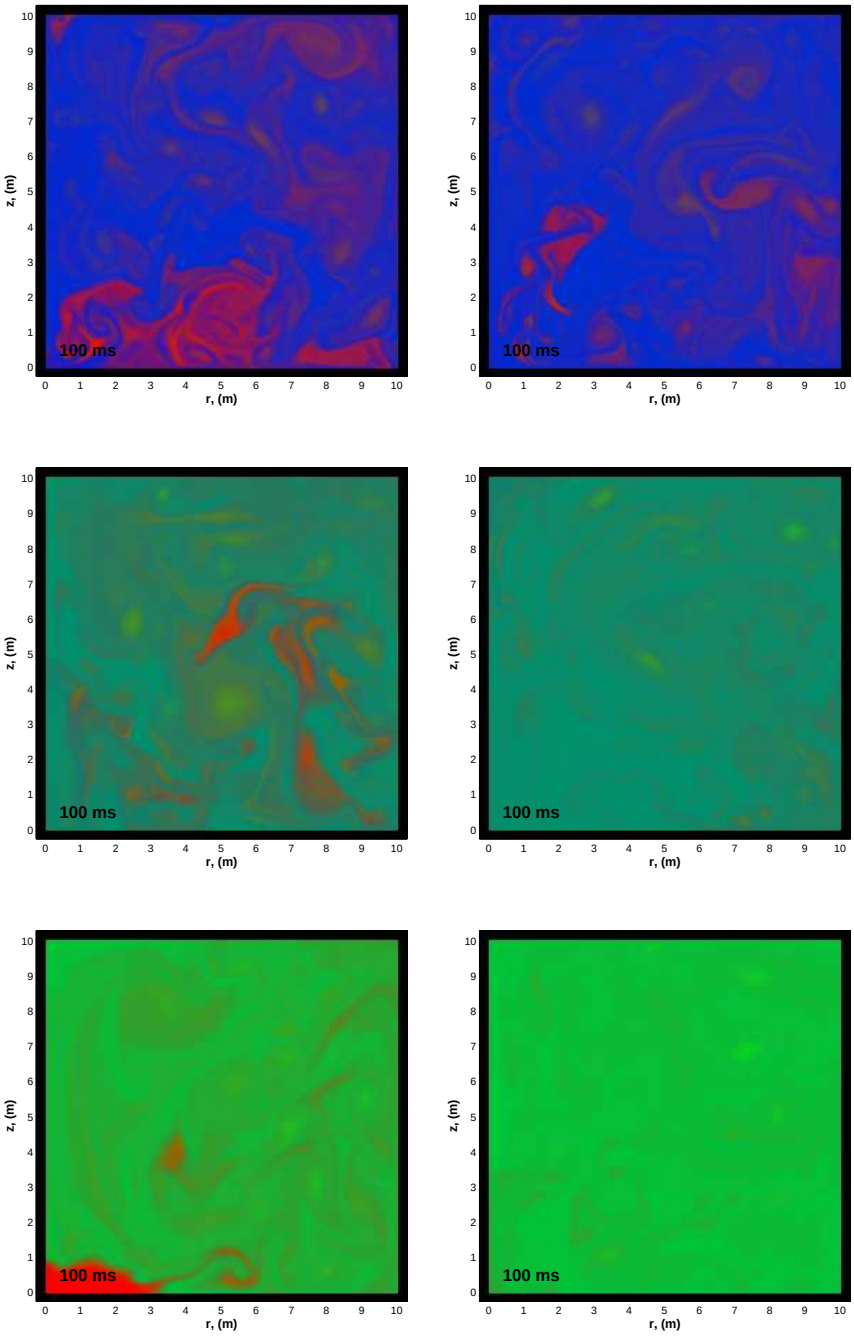

Figure IV.10: Mixture number fractions at $100ms$ for energy and mass flux matched cases. The left column corresponds to energy flux matched and the right column corresponds to mass flux matched. The rows are 125%, 150%, and 200% pure Xenon sound speed from top to bottom.

Table IV.6: Normalized thermal mixing residual for mass and energy fixed jets across sound speeds

η_T	100%	125%	150%	200%
Mass Fixed	0.359	0.548	0.164	0.066
Energy Fixed	0.359	0.545	0.138	0.047

volume average temperature than the pure Xenon case as shown in Table IV.4. Figures IV.11 and IV.12 show the volume average temperature for fixed mass and fixed energy jet cases respectively. Similar to the lower density cases for pure Xenon jets, the 125% Energy fixed case starts lower than the pure Xenon case but eventually the two cross. This is not unexpected because the Energy fixed cases include less mass and momentum within the jet. What is more surprising is the effectiveness of the Energy fixed case at 200% sound speed. With a jet mass of only 1.6 times that of the chamber gas, the volume average temperature can be reduced down to $826K$ from $3074K$ as shown in the included "No Jets" case. In the figures, the thin horizontal lines are the final mass average temperatures for the corresponding cases. They are included to show the volume average temperatures approaching these temperatures approximately asymptotically.

The definition of volume and mass average temperatures may be less appropriate for cases with Helium because regions with a higher number fraction Helium would be both colder and lower density. Assuming the pressure and temperature in the chamber relaxes faster than composition, the areas of high Helium concentration would be overrepresented by the volume average. However as seen in Figure IV.10, the higher fraction Helium cases have fewer fine scale structures indicating more complete mixing.

The temperature reduction using only 1.6 times the chamber gas mass would be less dramatic in steady state if the chamber gas remained a significant fraction of Helium between target injections. If the vacuum system reduced the number density in the chamber to the same level as before the first target, the

subsequent chamber gas mass would be considerably less because of the residual Helium in the mixture. For further progress to be made at evaluating steady state performance, results from "BUCKY" for a range of initial chamber gas compositions as well as the inclusion of reference design vacuum systems would be crucial.

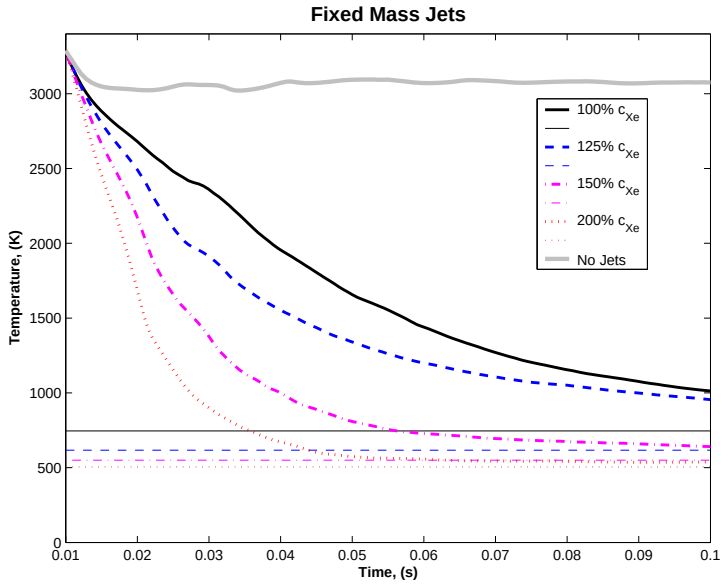

Figure IV.11: Fixed mass jet mixture volume average temperature versus final mass average temperature and no jet volume average temperature.

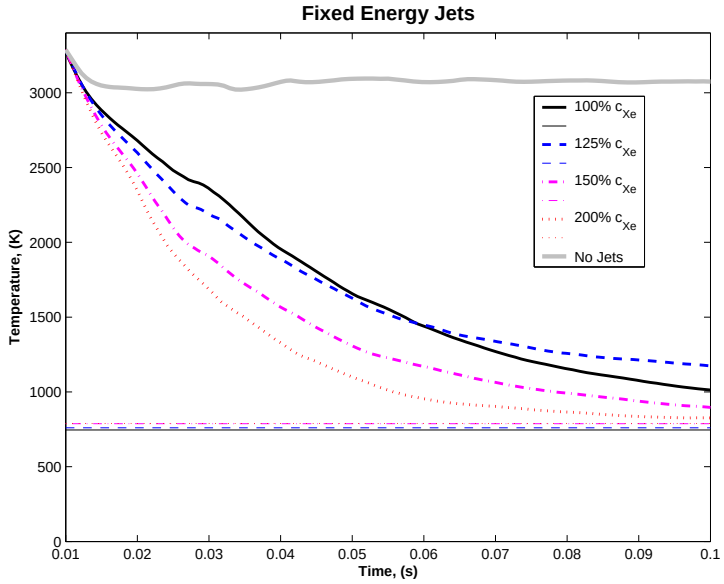

Figure IV.12: Fixed energy jet mixture volume average temperature versus final mass average temperature and no jet volume average temperature.

Chapter V

Conclusion

These preliminary results indicate that a significant reduction in chamber temperature may be obtained through the use of cold gas jets. This temperature reduction may be expedited with the inclusion of a small mass fraction of Helium. Several smaller higher density jets are also preferable to larger lower density jets. These results indicate that cold jets could be important method of enabling more rapid repetition rates and economically feasible reactors.

In order for this work to continue, the vacuum pumping capacity must be incorporated to ensure that the system could be used in steady state. The true effect of including cold jets on target tracking and survival is also dependent on final temperature, energy density, and velocity in a complex manner. The relative contributions of radiative and convective heat transfer as well as a turbulent velocity field must be considered to ensure a viable reference design.

Regardless of whether jets are included or not, an investigation into the effects of multi-species chamber gas should also be performed using radiation hydrodynamics codes such as "BUCKY". As shown in reference [8], Xenon was selected due its superiority to both Helium and deuterium as the chamber gas because of its better radiative performance. Without at least a small flux of pure Xenon, target waste products will eventually accumulate to significant levels within the chamber if a reactor is run at steady state. However, the Xenon mass flux required to main-

tain the chamber composition, though necessarily at least several times the mass flux of target material, would still be much smaller than the mass flux of the cold jets investigated here. Even with active cleaning of the chamber gas, some trace steady state levels of other gasses are inevitable. This is why it is important to ensure if and at what level these other gasses are detrimental to Xenon's radiative performance.

Though the Soret effect as applied obviously produces variations in the fluid composition particularly visible as bright green spots in Figure IV.8, further work should be done to isolate its relative contribution to the mixing and thermal relaxation of the chamber.

The extension of the fluid code also lays the groundwork for other future applications such as tracking ions as separate species. The multi-species framework would also be applicable in a broad range of fluids research including combustion and hypersonics.

Bibliography

[1] Abernathy, J.R., F. Rosenberger, *Soret diffusion and convective stability in a closed vertical cylinder*, Phys. Fluids, **24:3**, 377-381, (March 1981).

[2] Anderson, J., *Fundamentals of Aerodynamics*, Third Edition, McGraw-Hill, (2001).

[3] Bird, B., W. Stewart, E. Lightfoot, *Transport Phenomena*, John Wiley & Sons, Inc., (1960).

[4] Boehm, K., A. Raffray, *Transient thermo-mechanical behavior of a direct-drive target during injection in an inertial fusion energy chamber*, Fusion Engineering and Design, **82**, 265-290, (2007).

[5] Colella, P., *A Direct Eulerian MUSCL Scheme for Gas Dynamics*, SIAM J. SCI. STAT. COMPUT., **6:1**, 104-117, (1985).

[6] Colella, P., *Glimm's Method for Gas Dynamics*, SIAM J. SCI. STAT. COMPUT., **3:1**, 76-110, (1982).

[7] Dragojlovic, Z., F. Najmabadi, and M. Day, *An Embedded Boundary Method for Viscous, Conducting Compressible Flow*, Journal of Computational Physics, **216**, 37-51, (2006).

[8] Dragojlovic, Z. and F. Najmabadi, *Effect of Different IFE Chamber Gases and Pre-Ignition Conditions on Target Survival and Trajectory*, Preprint Manuscript, (2007).

[9] Dragojlovic, Z. and F. Najmabadi, *Simulation of IFE Chamber Dynamics Response by a Second Order Godunov Method with Arbitrary Geometry*, Fusion Science & Technology, **47**, 1152-1159, (May 2005).

[10] Gordon, S. and J. McBride, *Thermodynamic Data to 20 000 K for Monatomic Gases*, NASA/TP-1999-208523, (1999).

[11] Gutkowicz, D., M. Collins, J. Ross, *Rayleigh-Bénard instability in nonreactive binary fluids I. Theory*, Physics of Fluids **22:8**, 1443-1450, (1979).

[12] Herczynski, R., M. Tarczynski and Z. Walenta, *Shock Waves in Binary Gas Mixtures*, Proceedings of the Fifteenth International Symposium on Shock Tubes, Berkeley, California, (1985).

[13] Hirschfelder, J. O. , C. F. Curtiss, and R. B. Bird, *Molecular Theory of Gases and Liquids*, corrected printing, Wiley, (1964).

[14] Hurly, J., M. Moldover, *Ab Initio Values of the Thermophysical Properties of Helium as Standards*, J. Res. Natl. Inst. Stand. Technol., **105**, 667-688 (2000).

[15] LeVeque, R., *Numerical Methods for Conservation Laws*, Birkhäuser Verlag, Basel, (1990).

[16] Oran, E., J. Boris, *Numerical Simulation of Reactive Flow*, Elsevier Science Publishing Co., Inc., (1987).

[17] Pember, R., J. Bell, P. Colella, *et. al*, *An Adaptive Cartesian Grid Method for Unsteady Compressible Flow in Irregular Regions*, Computational Physics, **120:2**, 278-304, (1994).

[18] Reactor Design, *ChemKin® Software Theory Manual*, Release 4.0.2., (2005).

[19] Reactor Design, *ChemKin® Software Input Manual*, Release 4.0.2., (2005).

[20] Sherman, F., *Shock-wave structure in binary mixtures of chemically inert perfect gases*, Journal of Fluid Mechanics, **8**, 465-480, (1960).

[21] Srivastava, K., *Mutual Diffusion of Binary Mixtures of Helium Argon and Xenon at Different Temperatures*, Physica, **25**, 571-578 (1959).

[22] Tannehill, J., D. Anderson, R. Pletcher, *Computational Fluid Mechanics and Heat Transfer*, 2nd edition, Taylor & Francis, (1997).

[23] Touloukian, Y.S., editor, *Thermophysical Properties of Matter*, Plenum, New York, (1970).

[24] Vincenti, W. G. and C. H. Kruger Jr, *Introduction to Physical Gas Dynamics*, Krieger Publishing Company, (2002).